A&A 651, A115 (2021)
https://doi.org/10.1051/0004-6361/202039826

Astronomy & Astrophysics

LOFAR observations of galaxy clusters in HETDEX

Extraction and self-calibration of individual LOFAR targets

R. J. van Weeren[1], T. W. Shimwell[2,1], A. Botteon[1], G. Brunetti[3], M. Brüggen[4], J. M. Boxelaar[1], R. Cassano[3], G. Di Gennaro[1], F. Andrade-Santos[5], E. Bonnassieux[6], A. Bonafede[6,3], V. Cuciti[4], D. Dallacasa[3,6], F. de Gasperin[4], F. Gastaldello[7], M. J. Hardcastle[8], M. Hoeft[9], R. P. Kraft[5], S. Mandal[1], M. Rossetti[7], H. J. A. Röttgering[1], C. Tasse[10,11,12], and A. G. Wilber[13,4]

[1] Leiden Observatory, Leiden University, PO Box 9513, 2300 RA Leiden, The Netherlands
e-mail: rvweeren@strw.leidenuniv.nl
[2] ASTRON, The Netherlands Institute for Radio Astronomy, Postbus 2, 7990 AA Dwingeloo, The Netherlands
[3] INAF-Istituto di Radioastronomia, Via Gobetti 101, 40129 Bologna, Italy
[4] University of Hamburg, Hamburger Sternwarte, Gojenbergsweg 112, 21029 Hamburg, Germany
[5] Harvard-Smithsonian Center for Astrophysics, 60 Garden Street, Cambridge, MA 02138, USA
[6] Dipartimento di Fisica e Astronomia, Università di Bologna, Via P. Gobetti 93/2, 40129 Bologna, Italy
[7] INAF-IASF Milano, Via A. Corti 12, 20133 Milano, Italy
[8] Centre for Astrophysics Research, University of Hertfordshire, College Lane, Hatfield AL10 9AB, UK
[9] Thüringer Landessternwarte, Sternwarte 5, 07778 Tautenburg, Germany
[10] GEPI, Observatoire de Paris, CNRS, Université Paris Diderot, 5 place Jules Janssen, 92190 Meudon, France
[11] Centre for Radio Astronomy Techniques and Technologies, Department of Physics and Electronics, Rhodes University, Grahamstown 6140, South Africa
[12] USN, Observatoire de Paris, CNRS, PSL, UO, Nançay, France
[13] Curtin Institute of Radio Astronomy, 1 Turner Avenue, Technology Park, Bentley, WA 6102, Australia

Received 2 November 2020 / Accepted 21 April 2021

ABSTRACT

Diffuse cluster radio sources, in the form of radio halos and relics, reveal the presence of cosmic rays and magnetic fields in the intracluster medium (ICM). These cosmic rays are thought to be (re)accelerated through the ICM turbulence and shock waves generated by cluster merger events. Here we characterize the presence of diffuse radio emission in known galaxy clusters in the HETDEX Spring Field, covering 424 deg^2. For this, we developed a method to extract individual targets from LOFAR observations processed with the LoTSS DDF-pipeline software. This procedure enables improved calibration as well as the joint imaging and deconvolution of multiple pointings of selected targets. The calibration strategy can also be used for LOFAR low-band antenna and international-baseline observations. The fraction of *Planck* PSZ2 catalog clusters with any diffuse radio emission apparently associated with the ICM is 73 ± 17%. We detect a total of ten radio halos and twelve candidate halos in the HETDEX Spring Field. Of these ten radio halos, four are new discoveries, two of which are located in PSZ2 clusters. Five clusters host radio relics, two of which are new discoveries. The fraction of radio halos in *Planck* PSZ2 clusters is 31 ± 11%, or 62 ± 15% when including the candidate radio halos. Based on these numbers, we expect that there will be at least 183 ± 65 radio halos found in the LoTSS survey in PSZ2 clusters, in agreement with past predictions. The integrated flux densities for the radio halos were computed by fitting exponential models to the radio images. From these flux densities, we determine the cluster mass (M_{500}) and Compton Y parameter (Y_{500}) 150 MHz radio power ($P_{150\,\mathrm{MHz}}$) scaling relations for *Planck* PSZ2-detected radio halos. Using bivariate correlated errors and intrinsic scatter orthogonal regression, we find slopes of 6.13 ± 1.11 and 3.32 ± 0.65 for the M_{500}–$P_{150\,\mathrm{MHz}}$ and M_{500}–$P_{150\,\mathrm{MHz}}$ relations, respectively. These values are consistent with the results of previous works.

Key words. galaxies: clusters: general – galaxies: clusters: intracluster medium – large-scale structure of Universe – radiation mechanisms: non-thermal – X-rays: galaxies: clusters

1. Introduction

Radio observations have revealed the presence of megaparsec-scale radio sources associated with the intracluster medium (ICM) in a growing number of galaxy clusters. This indicates that the ICM is filled with cosmic ray (CR) electrons and magnetic fields. Diffuse cluster radio sources are commonly divided into radio relics (radio shocks), giant halos, and mini-halos (for reviews, see Feretti et al. 2012; Brunetti & Jones 2014; van Weeren et al. 2019). Importantly, the short lifetime ($\sim 10^{7-8}$ yr) of the CR electrons implies that some form of in situ particle (re)acceleration is required to explain the megaparsec extent of these sources.

Giant radio halos are megaparsec-size sources that approximately follow the X-ray emission from the thermal ICM. They are predominantly found in merging clusters (Cassano et al. 2010b). The radio power of giant halos correlates with cluster mass (e.g., Cassano et al. 2013), and often used mass proxies are the cluster's X-ray luminosity (L_X) or integrated Compton Y parameter. The upper limits derived for clusters that are dynamically relaxed are under-luminous with respect to these correlations (e.g., Brunetti et al. 2007; Cassano et al. 2013). The

fraction of clusters with radio halos is about 30% (Venturi et al. 2008; Kale et al. 2013, 2015) for $L_{X,0.1-2.4\,keV} > 5 \times 10^{44}$ erg s^{-1} clusters in the range $0.2 < z < 0.4$. For the most massive clusters ($\sim 10^{15}\,M_{\odot}$), the occurrence fraction is as high as ~80%, and there is evidence that this fraction decreases for lower mass clusters (Cuciti et al. 2015).

Two main classes of models have been proposed for the origin of radio halos. In the turbulent reacceleration model, particles are reaccelerated by merger-induced magneto-hydrodynamical turbulence (Brunetti et al. 2001; Petrosian 2001; Brunetti & Lazarian 2007; Miniati 2015). In the hadronic model, the radio emission is produced by secondary electrons that arise from hadronic collisions (e.g., Dennison 1980; Blasi & Colafrancesco 1999; Dolag & Enßlin 2000). Most observational evidence nowadays is in favor of the turbulent reacceleration model. This evidence includes the discovery of radio halos with ultra-steep radio spectra (USSRHs; e.g., Brunetti et al. 2008) and the non-detection of gamma ray emission from the Coma cluster at the level that would be necessary to generate the observed radio emission (Brunetti et al. 2012, 2013, 2017; Ackermann et al. 2016). Models for radio halos that invoke a combination of turbulent reacceleration and the generation of secondary particles that are consistent with gamma ray limits have also been proposed (e.g., Brunetti & Lazarian 2011; Pinzke et al. 2017; Brunetti et al. 2017).

Radio mini-halos are smaller sized halos (~200–500 kpc) that are exclusively found in relaxed cool-core clusters. Recently, Giacintucci et al. (2017) found that mini-halos are rather common in massive cool-core clusters; about 80% of such clusters host them. The radio emission from mini-halos surrounds the central active galactic nucleus (AGN) associated with the brightest cluster galaxy (BCG). Similar to giant radio halos, some form of in situ acceleration is required to power them (e.g., Gitti et al. 2004; Giacintucci et al. 2014). Mini-halos have been explained by hadronic scenarios (e.g., Pfrommer & Enßlin 2004; Fujita et al. 2007; Keshet & Loeb 2010; Fujita & Ohira 2013) or by turbulent reacceleration induced by gas sloshing motions (Mazzotta & Giacintucci 2008; ZuHone et al. 2013).

Radio relics are polarized, elongated sources found in galaxy cluster outskirts (e.g., Enßlin et al. 1998). They have sizes that can extend up to about 2 Mpc. High-resolution observations show that radio relics often have filamentary morphologies (e.g., Bagchi et al. 2006; Di Gennaro et al. 2018; Rajpurohit et al. 2020, 2018). These sources trace ICM shock waves with low to moderate Mach numbers (e.g., Finoguenov et al. 2010; Akamatsu & Kawahara 2013; Ogrean & Brüggen 2013; Shimwell et al. 2015). The physical mechanisms by which particles are (re)accelerated at shocks are still being debated. One such possibility is the acceleration of particles at shocks via the diffusive shock acceleration (DSA) mechanism (e.g., Blandford & Eichler 1987; Jones & Ellison 1991; Malkov 2001). However, this mechanism is thought to be rather inefficient for weak ICM shocks if particles are accelerated from the thermal pool, and it fails to explain the observed radio power and spectral indices in a number of cases (e.g., Pinzke et al. 2013; Vazza & Brüggen 2014; Vazza et al. 2016; van Weeren et al. 2016a; Botteon et al. 2020a). It has therefore been proposed that some form of reacceleration of preexisting fossil CR electrons takes place (e.g., Markevitch et al. 2005; Giacintucci et al. 2008; Kang & Ryu 2011; Kang et al. 2012; van Weeren et al. 2016a; Botteon et al. 2016a). Observations provide support for this model, in which the fossil CRs originate from the tails and lobes of radio galaxies (Bonafede et al. 2014a; Shimwell et al. 2015; van Weeren et al. 2017). It should be noted, however, that for some relics the DSA of thermal pool electrons seems to be sufficient to explain their luminosity (e.g., Botteon et al. 2016b; Locatelli et al. 2020).

Low-frequency observations provide important information about particle acceleration processes. The turbulent reacceleration model for radio halos predicts that the occurrence rate of halos should be higher at low frequencies (Cassano 2010; Cassano et al. 2012). Radiative losses of CR electrons limit the acceleration by turbulence via second-order Fermi mechanisms, causing a break in the energy spectrum of these electrons (Cassano et al. 2004, 2006; Cassano & Brunetti 2005; Brunetti et al. 2008). This in turn results in a synchrotron spectrum that becomes steeper in situations where the amount of turbulent energy is smaller (less powerful mergers) or the energy losses are more significant (higher redshift).

Another important role of low-frequency observations is to probe the connection between reacceleration processes and fossil radio plasma. Because of synchrotron and inverse Compton (IC) losses, relativistic electrons emit almost exclusively at low frequencies as they age. These seed fossil CR particles are a critical ingredient in both shock and turbulent reacceleration models. Possible examples of revived fossil plasma, by compression (Enßlin & Gopal-Krishna 2001; Enßlin & Brüggen 2002) or other mechanisms (e.g., Markevitch et al. 2005), have been detected in some clusters (e.g., Slee et al. 2001; van Weeren et al. 2017; de Gasperin et al. 2017; Mandal et al. 2020). However, this is probably just the tip of the iceberg.

Finally, recent Low Frequency Array (LOFAR) observations have entered uncharted territories, discovering the existence of radio bridges that connect pairs of massive and pre-merging clusters (Govoni et al. 2019; Botteon et al. 2020c). One possibility is that these bridges originate from second-order Fermi acceleration mechanisms that are powered by the turbulence that fills these vast regions (Brunetti & Vazza 2020).

The LOFAR Two-metre Sky Survey (LoTSS; Shimwell et al. 2017) is a deep 120–168 MHz survey that will cover the entire northern sky when completed. This survey is carried out with the high-band antenna (HBA) stations of LOFAR (van Haarlem et al. 2013). The nominal sensitivity of this survey is 0.1 mJy beam^{-1} at a resolution of 6″. Data Release 1 (DR1) covers 424 deg^2 in the region of the HETDEX Spring Field (Shimwell et al. 2019). Given its unprecedented survey depth at low frequencies, its resolution, and its sky coverage, LoTSS will play an important role in determining the statistics of diffuse cluster sources. In this paper we present the first results on a full sample of galaxy clusters in the LoTSS DR1 area using improved calibration techniques. This is required to properly study extended low-surface-brightness cluster sources. The outline of this paper is as follows. In Sect. 2 we describe the procedure we have developed to extract and recalibrate targets of interest from the LoTSS data products. The sample selection is described in Sect. 3. The results are presented in Sect. 4, and we end with a discussion and conclusions in Sects. 5 and 6.

Throughout this paper we assume a Lambda cold dark matter (ΛCDM) cosmology with $H_0 = 70\,km\,s^{-1}\,Mpc^{-1}$, $\Omega_m = 0.3$, and $\Omega_\Lambda = 0.7$. All images are in the J2000 coordinate system. For the sign convention of the spectral index (α), we use $S_\nu \propto \nu^\alpha$, where S is the flux density.

2. Extraction and recalibration

We utilized LOFAR observations that were taken as part of the LoTSS survey. These are typically 8 h observations. The pointing centers of these observations were placed with the aim

of obtaining close to uniform sensitivity coverage of the northern sky. The LoTSS survey design and the observations are discussed in detail in Shimwell et al. (2017, 2019).

2.1. Extraction

The LoTSS processing pipeline (DDF-PIPELINE) delivers images of the full field of view (FoV) of the Dutch LOFAR HBA stations (Tasse 2014a,b; Shimwell et al. 2019). These images have a resolution of 6″ and an rms noise level on the order of 100 μJy beam^{-1}. This is achieved by correcting for the direction-dependent effects (DDEs) in the LOFAR data (due to the ionosphere and imperfect station beam models). For LoTSS, DDE corrections are applied toward 45 directions (facets). The DDF-PIPELINE is optimized to create images of LOFAR's full FoV and carry out survey science. The latest version of the DDF-PIPELINE (version 2), which we employed in this work, is described in Tasse et al. (2021). Version 2 of the pipeline is a major improvement over version 1, which was used for public DR1 data. The images from DR1 are generally not suitable for studying extended low-surface-brightness cluster sources (see Sect. 3.7 in Shimwell et al. 2019).

The individual images produced by the DDF-PIPELINE[1] are very large, 20 000 × 20 000 pixels with a pixel size of 1.5″. This makes reimaging with different settings, for example *uv*-ranges, weighting schemes, and deconvolution algorithms, expensive. The tessellation of the sky into 45 calibration facets is done in a fully automated way. The DDE calibration takes all sources in a facet into account, assuming there are no DDEs inside a facet. This means that for certain specific targets of interest the facet layout is not optimal. Experience with various faceting schemes has shown that it is often possible to further improve the quality of the DDE calibration for a specific target (sometimes at the expense of other sources).

To allow flexible reimaging and to optimize the calibration toward targets of interest, we extended the DDF-PIPELINE with an optional step. In this step, all sources, apart from those in a specific user-defined region, are subtracted from the visibility data after their DDE calibration solutions are applied. The model visibility prediction is done with the DDFacet imager (Tasse et al. 2018). An important requirement for extraction is that the region of interest be quite small, at least roughly similar to the size of the original facet, though ideally smaller. This is directly related to the fact that we want to improve the DDE calibration, which was limited by the original facet size and the "incorrect" assumption that the DDE correction is constant across that entire facet. This requirement competes with another requirement, that there be sufficient flux density available for calibration. A smaller extraction region will have less flux density available for the calibration.

2.2. Phase shifting and averaging

After subtracting all sources (clean components) from the *uv*-data, apart from those in the region of interest, we phase shifted the *uv*-data. The new phase center was placed at the center of the region of interest, that is, the region where the sources were kept. In practice, we used DS9 (Joye & Mandel 2003) region files, which can be easily generated. After phase shifting, the data were averaged in time and frequency. The extracted region has a small angular extent, and thus bandwidth and time smearing are not an issue. By default, the data were averaged to 16 s and 0.39 MHz. With these averaging parameters, the size of the data set is reduced by a factor of eight. The visibility data were compressed using Dysco to further reduce data size by about a factor of four (Offringa 2016). Additional averaging is often allowed from the point of bandwidth and time smearing, but we found that more averaging can hinder ionospheric calibration. Optionally, additional radio frequency interference (RFI) flagging is carried out with AOFlagger on the output data (Offringa 2010; Offringa et al. 2010, 2012).

When the data were shifted to the new phase center, we also corrected for the LOFAR station beam response in this direction. Additionally, the visibility weights set by the DDF-pipeline (for details, see Bonnassieux et al. 2018) were updated. They were multiplied by a factor inversely proportional to the station beam response. In this way, we were able to optimally combine observations from multiple pointing centers with joint imaging and deconvolution. Combining visibility data in this way is allowed because the beam correction is close to constant across the small region that is extracted[2].

2.3. Self-calibration

The next step in the "extraction" process for a target of interest is to self-calibrate the data. The starting point of this step involves one or more phase-shifted and averaged data sets for the target of interest, each one corresponding to a different observation with a potentially different pointing center. The direction-independent (DI) full Jones calibrations were carried over from the DDF-pipeline. We did not carry over the DDE solutions, in order to avoid the issue with the "negative halos" described in Tasse et al. (2021). These halos are created when regularizing the DDE calibration solutions afterward, by fitting a functional form to the phase solutions and replacing the solutions with the fit. This problem does not occur when directly solving for the functional form on the visibility data, as done here.

The self-calibration steps consisted of three rounds of "tecandphase" calibration with DPPP (van Diepen & Dijkema 2018). This was followed by several rounds of diagonal (i.e., *XX* and *YY*) gain calibration using a longer solution interval. The shorter timescale tecandphase solutions were pre-applied when solving for the diagonal gains. This scheme somewhat mimics the facet-calibration scheme (van Weeren et al. 2016b) as well as the DDF-pipeline, which also pre-applies fast total electron content (TEC) and phase solutions before solving for slow gain solutions. The diagonal gain solutions were filtered for outliers with LoSoTo (de Gasperin et al. 2019). The solution intervals were automatically determined based on the amount of apparent compact source flux in the extracted region. Solution intervals for the tecandphase calibration were between 16 s and 48 s. Solution intervals for the diagonal gains were between 16 min and 48 min. All solution intervals were set per observation since the apparent flux in the target of interest region can differ. Solution intervals along the frequency axis for the diagonal gains were between 2 MHz and 6 MHz. For HBA data, a minimum of 0.3 Jy compact (apparent) source flux was needed for the self-calibration steps to converge well. If needed, all solution intervals could be manually controlled by the user. An overview of the parameters used is given in Table 1.

[1] https://github.com/mhardcastle/ddf-pipeline

[2] If that approximation did not hold, we used the image domain gridding algorithm, which corrects each phase-rotated data set with the correct beam response (van der Tol et al. 2018).

Table 1. Default imaging and calibration parameters for HBA extraction.

Parameter	Value
Inner *uv*-range (calibration)	350 [(a)]
Inner *uv*-range (imaging, λ)	80
Clean mask threshold (sigma)	5
Pixelsize (arcsec)	1.5
Briggs robust weighting	−0.5
Channelsout [(b)]	6

Notes. [(a)]Increased to 750λ for targets with extended low-surface-brightness emission. [(b)]`WSClean` wideband deconvolution setting.

The imaging was done with `WSClean` (Offringa et al. 2014) in the wideband joint deconvolution mode ("channelsout" 6 default), optionally with multi-scale clean (Offringa & Smirnov 2017). The `DDFacet` imager (Tasse et al. 2018) could also have been used instead of `WSClean`. By default, Briggs (i.e., robust) weighting −0.5 was used. The imaging included automatic clean masking from the `DDF-pipeline`, with a default 5σ threshold. Baseline-based averaging was also employed when imaging for performance. This typically speeds up the imaging step by about a factor of 1.5–2. An inner *uv*-cut of 80λ was used in the imaging. For the calibration, a default inner *uv*-cut of 350λ (corresponding to 0.65°) was employed. This value is a compromise between the number of baselines in the calibration and the increased difficulty of modeling very extended structures.

In Fig. 1 we show an example of the self-calibration process. The top panel shows the first image before any self-calibration. We note that here two different observations (L254483 and L719874), with different pointing centers, are jointly imaged and deconvolved. The only calibration that is applied here is the DI calibration from the `DDF-pipeline`. In the middle panel we show the result after three rounds of tecandphase self-calibration. The radial patterns, caused by the ionosphere, disappear after this calibration. In the bottom panel we show the results after additional diagonal gain calibration. The diagonal gain calibration corrects for the imperfect knowledge of the station beam response or other slowly varying gain errors.

In Fig. 2 we display two comparisons between the default LoTSS mosaics and the newly extracted and recalibrated targets (in this case, the clusters Abell 1430 and 1294). As can be seen, the calibration for the targets of interest has improved. The improvement is the result of shrinking the size of the calibration region so that a nearby bright compact source is better calibrated. The extraction and self-calibration scheme has already been successfully applied in various recent works (e.g., Botteon et al. 2020b,c; Mandal et al. 2020; Hardcastle et al. 2019; Cassano et al. 2019; Gu et al. 2019).

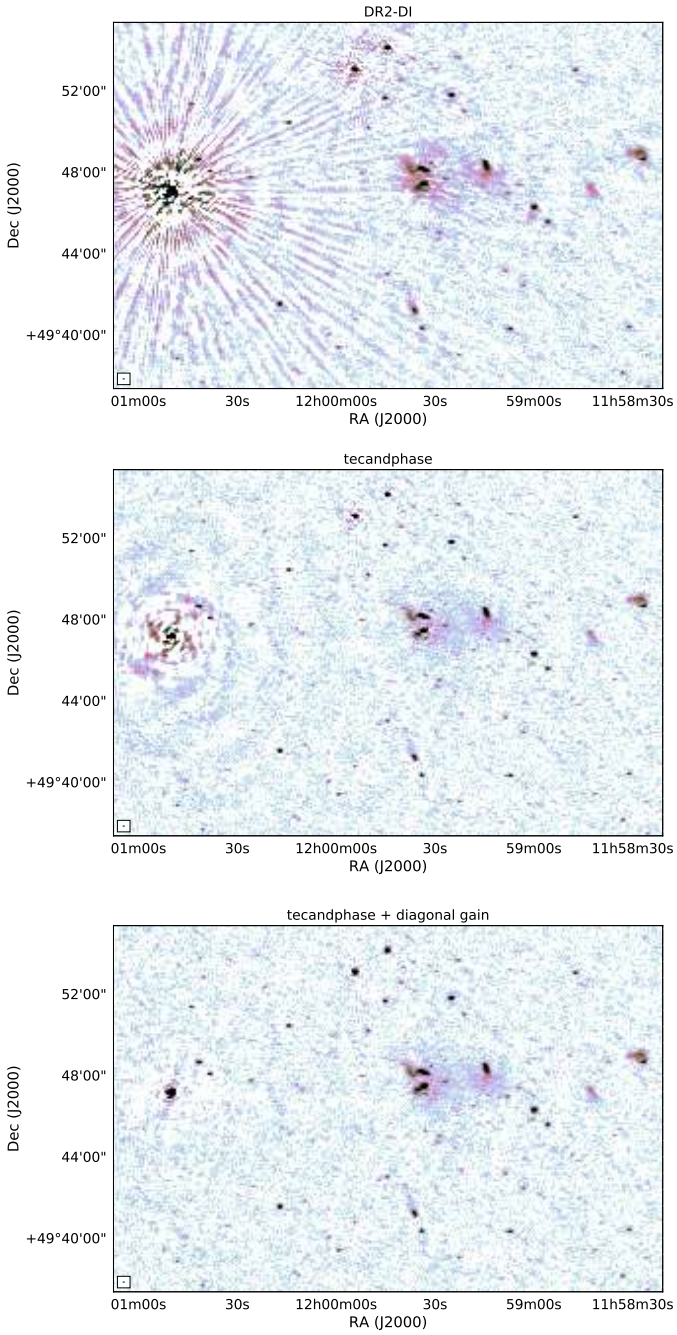

Fig. 1. Subsequent improvement during self-calibration on the extracted data of the cluster Abell 1430. *Top panel*: starting point of this process: the `DDF-pipeline` (v2) DI calibration. *Middle panel*: results after the `DPPP` tecandphase calibration. *Bottom panel*: final image after the `DPPP` diagonal gain calibration.

2.4. Other usage

The self-calibration step has been designed in such a way that it can also be carried out on other (non-LoTSS) LOFAR-extracted data sets. It offers full flexibility for the various effects that can be solved for in `DPPP`, including constraint solves. For example, it can force the gains to be smooth along the frequency axis or enforce the same solutions for certain stations. The self-calibration step has been successfully used on LOFAR HBA international-baseline data and on the low-band antenna (LBA) observations. Figure 3 shows an example of it working on LBA and international-baseline data.

3. HETDEX DR1 area galaxy cluster sample

We applied the extraction scheme described in Sect. 2.1 to a sample of galaxy clusters that fall inside the LOFAR DR1 area (Shimwell et al. 2017, 2019). We selected clusters from the all-sky PSZ2 *Planck* catalog (Planck Collaboration XXVII 2016) of Sunyaev–Zel'dovich (SZ) sources (see Fig. 4). This sample of 26 clusters serves as the primary sample for our statistical investigations and is listed in Table 2.

In addition to the SZ-selected sample, we compiled a secondary sample by visually inspecting the LoTSS images at the

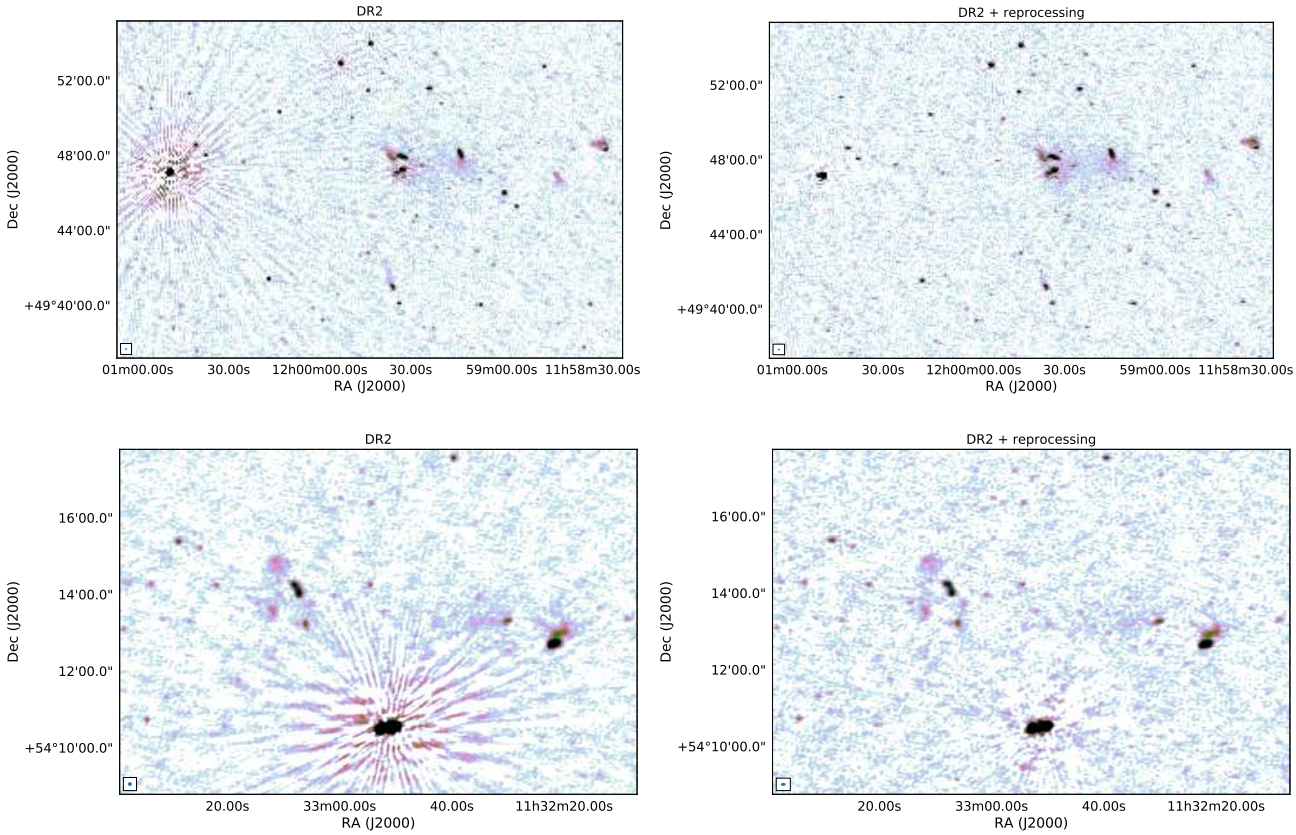

Fig. 2. Comparison between the LoTSS DR2 mosaics and the extracted and recalibrated images for the clusters Abell 1430 (*top panels*) and Abell 1294 (*bottom panels*). For both clusters, optimizing the calibration toward a nearby bright compact source improved the image quality. These errors in the LoTSS DR2 mosaics were caused by the spatially varying ionosphere. We note that the DR2 pipeline could have achieved more or less the same results with a different facet layout (but at the cost of reducing image quality in other directions).

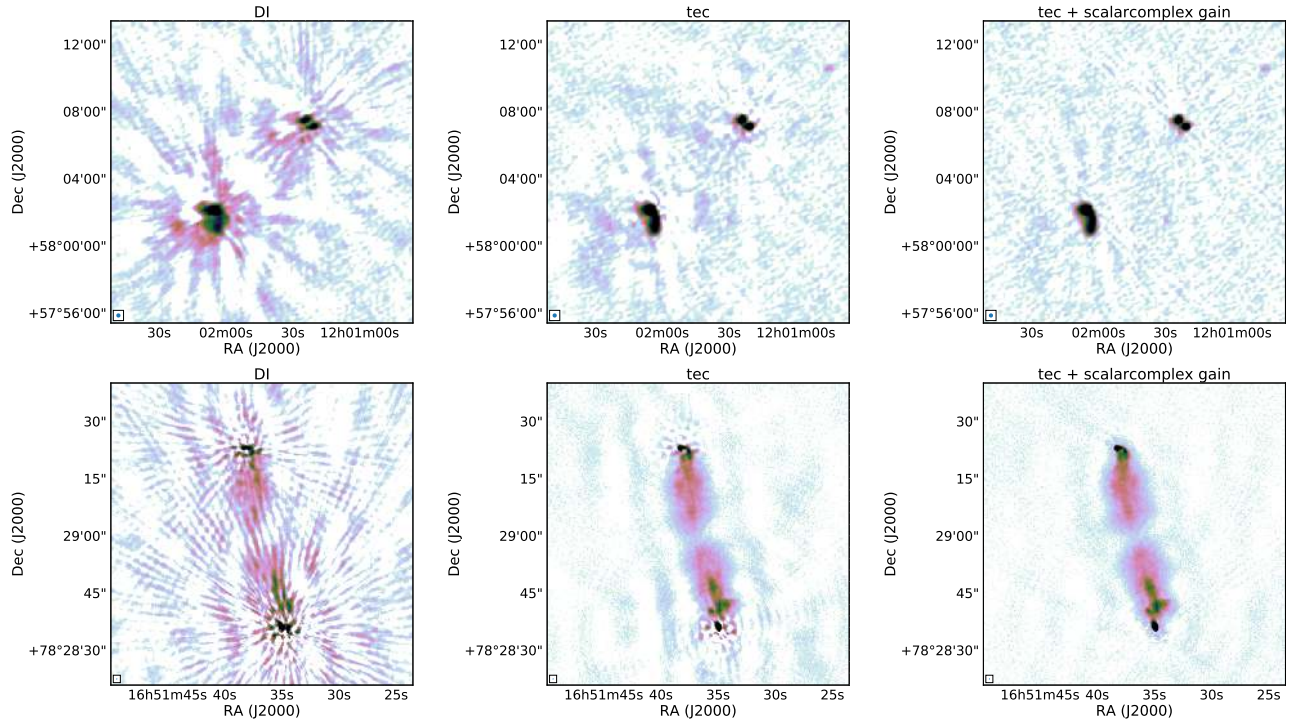

Fig. 3. Improvement during self-calibration on extracted data. *Left column*: starting point of this process: a DI calibrated image. *Middle column*: results after DPPP TEC calibration, with all LOFAR core stations forced ("antenna constraint" solve) to have the same solution. *Right column*: final image after DPPP scalarcomplex gain calibration. *Top row*: 43–67 MHz LBA data. *Bottom row*: LOFAR international-baseline 120–168 MHz HBA data.

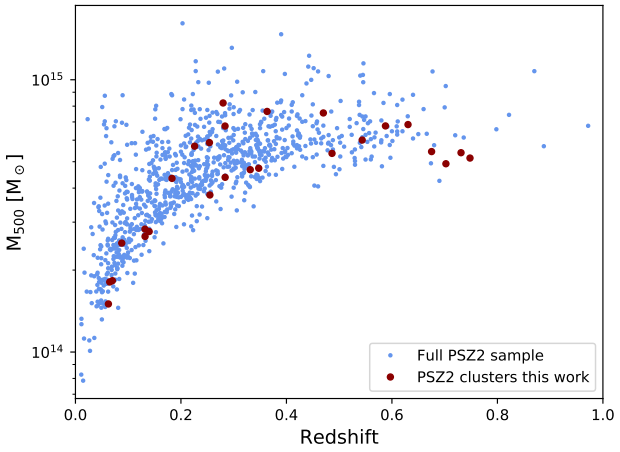

Fig. 4. Redshift-mass distribution of PSZ2 clusters. Clusters that are located in the HETDEX DR1 area are indicated with dark red points.

locations of known clusters for the presence of diffuse emission and possible revived fossil plasma sources. Clusters in this sample with (candidate) extended radio emission are from the Abell and Zwicky (Abell 1958; Zwicky et al. 1961; Corwin 1974), MCXC (Piffaretti et al. 2011), GMBCG (Hao et al. 2010), MaxBCG (Koester et al. 2007), and WHL (Wen et al. 2012) catalogs.

To search for diffuse radio emission, we produced images with the emission from compact sources subtracted. This was done by first imaging the calibrated data sets with a *uv*-cut corresponding to a physical scale of 0.4 Mpc. This model was subsequently subtracted from the visibility data.

3.1. Flux density measurements

The flux density measurements for all sources, except radio halos, were done manually by placing a polygon around the sources and integrating the flux density. The uncertainty on the flux density is given by

$$\sigma_S^2 = N_{\rm beams}\sigma_{\rm rms}^2 + \sigma_{\rm sub}^2 + (f \times S)^2\,, \quad (1)$$

where $f = 0.2$ is the absolute flux-scale uncertainty (Shimwell et al. 2019), $N_{\rm beams}$ the number of beams covering the source, $\sigma_{\rm rms}$ the map noise, and $\sigma_{\rm sub}$ the uncertainty due to compact source subtraction. The first two terms of Eq. (1) represent the statistical uncertainty on the flux density measurement. The uncertainty on the compact source subtraction is given by

$$\sigma_{\rm sub}^2 = \sum_i N_{{\rm beams},i}\sigma_{\rm rms}^2, \quad (2)$$

where the sum is taken over all the i sources that were subtracted in the polygon.

The radio halo integrated flux densities were determined by fitting exponential profiles (Murgia et al. 2009) to the radio images of the form

$$I(r) = I_0 {\rm e}^{-r/r_e}, \quad (3)$$

where r_e is a characteristic e-folding radius and I_0 is the central surface brightness. We used the image where compact sources were subtracted. Also, all images were smoothed to a beam size corresponding to a physical scale of 50 kpc at the cluster's redshift. For the fitting we used `Halo-FDCA`[3], which is described in Boxelaar et al. (2021). Extended sources, such as large-tailed radio galaxies, were masked during the fitting (in case they were not fully subtracted). The flux density was integrated to a radius of $3r_e$, as proposed by Murgia et al. (2009). Integrating up to a radius of $3r_e$ results in 80% of the flux density when compared to using an infinite radius. This also avoids, to some extent, the uncertainties related to the extrapolation of the profile to large radii where the radio surface brightness is below the detection limit. The fitting uses a Markov chain Monte Carlo (MCMC) method to determine the radio halo parameters and associated uncertainties. The uncertainties due to masking parts of the halo are taken into account when computing the uncertainties. For some clusters, when specifically mentioned in Sect. 4, we fitted an elliptical exponential model (see Boxelaar et al. 2021). In these cases, a major and minor characteristic e-folding radius and position angle were determined. This was done for radio halos that clearly display an elongated, rather than circular, shape. In this work we did not use the skewed (asymmetric) models that are available in `Halo-FDCA`. A full exploration of radio halo fitting models and methods is beyond the scope of this work.

For the total uncertainty on the radio halo integrated flux density, we added the uncertainty from the MCMC (statistical errors) and flux calibration uncertainty in quadrature.

[3] https://github.com/JortBox/Halo-FDCA

3.2. X-ray observations

We searched the *Chandra* and *XMM-Newton* archives for the available X-ray observations of the clusters in the sample. When available, data were retrieved and processed with CIAO 4.11 using CalDB v4.8.2 and SAS v16.1.0 following standard data reduction recipes. We used the time periods of the observations cleaned by an anomalously high background to produce cluster exposure-corrected images in the 0.5−2.0 keV band. These images were used to investigate the connection between the thermal and nonthermal components in the ICM.

4. Results

Here we describe the LOFAR results for the individual clusters. By default, images were made using robust weighting −0.5 (Briggs 1995). An overview of the image properties is given in Table B.1. In addition, images at lower resolution were produced using a Gaussian taper to down weight the visibilities from longer baselines. Images with the emission from compact sources subtracted are also shown for some clusters.

We detect a total of ten radio halos and twelve candidate halos. Five clusters host radio relics. Of these ten radio halos, four are new discoveries, two of which are located in PSZ2 clusters. Two PSZ2 clusters host newly discovered radio relics. All but one of the candidate radio halos are reported for the first time. The classification of diffuse sources is summarized in Table 3. For optical overlays, we used Pan-STARRS *gri* images (Chambers et al. 2016). Descriptions and images of the clusters for which no diffuse emission was detected are given in Appendix A. Here we also include clusters that have already been discussed in the literature and for which our presented LOFAR images do not reveal significant new information.

4.1. PSZ2 G080.16+57.65, Abell 2018

Abell 2018 is relatively nearby cluster located at $z = 0.0878$. The Pan-STARRS *gri* image reveals a number of central galaxies without a clear dominant BCG. The cluster has a low PSZ2 mass

Table 2. HETDEX DR1 area cluster sample.

Cluster	Alternative name(s)	RA (h min s)	Dec (° ′ ″)	Redshift	$M_{500,SZ}$ (10^{14} $M_\odot$)
PSZ2 G080.16+57.65	Abell 2018	15 01 08	+47 16 37	0.0878	$2.51^{+0.20}_{-0.21}$
PSZ2 G084.10+58.72		14 49 01	+48 33 24	0.7310	$5.40^{+0.62}_{-0.62}$
PSZ2 G086.93+53.18	WHL J228.466+52.8333	15 14 00	+52 48 14	0.6752	$5.45^{+0.50}_{-0.52}$
PSZ2 G087.39+50.92	[WH2015] 0986	15 26 33	+54 09 08	0.7480	$5.16^{+0.53}_{-0.60}$
PSZ2 G088.98+55.07		14 59 01	+52 49 01	0.7023	$4.92^{+0.60}_{-0.64}$
PSZ2 G089.52+62.34	Abell 1904 RX J1422.1+4831	14 22 13	+48 29 54	0.0701	$1.83^{+0.19}_{-0.20}$
PSZ2 G095.22+67.41	RXC J1351.7+4622 MCXC J1351.7+4622	13 51 45	+46 22 00	0.0625	$1.50^{0.21+}_{-0.22}$
PSZ2 G096.14+56.24	Abell 1940 RX J1435.4+5508	14 35 21	+55 08 29	0.1398	$2.77^{+0.24}_{-0.26}$
PSZ2 G098.44+56.59	Abell 1920 RX J1427.4+5545	14 27 25	+55 45 02	0.1318	$2.83^{+0.28}_{-0.26}$
PSZ2 G099.86+58.45	WHL J141447.2+544704 WHL J213.697+54.7844	14 14 43	+54 47 01	0.6160	$6.85^{+0.48}_{-0.49}$
PSZ2 G106.61+66.71		13 30 29	+49 08 48	0.3314	$4.67^{+0.55}_{-0.57}$
PSZ2 G107.10+65.32	Abell 1758	13 32 35	+50 29 09	0.2799	$8.22^{+0.27}_{-0.28}$
PSZ2 G111.75+70.37	Abell 1697 RXC J1313.1+4616	13 13 03	+46 16 52	0.1830	$4.34^{+0.32}_{-0.33}$
PSZ2 G114.31+64.89	Abell 1703	13 15 05	+51 49 02	0.2836	$6.76^{+0.36}_{-0.38}$
PSZ2 G114.99+70.36	Abell 1682	13 06 50	+46 33 27	0.2259	$5.70^{+0.35}_{-0.35}$
PSZ2 G118.34+68.79	ZwCl 1259.0+4830 [WH2015] 0746	13 01 24	+48 14 31	0.2549	$3.77^{+0.45}_{-0.52}$
PSZ2 G123.66+67.25	Abell 1622 ZwCl 1247.2+5008	12 49 41	+49 52 18	0.2838	$4.38^{+0.50}_{-0.52}$
PSZ2 G133.60+69.04	Abell 1550	12 29 02	+47 37 21	0.2540	$5.88^{+0.38}_{-0.42}$
PSZ2 G135.17+65.43	WHL J121912.2+505435	12 19 12	+50 54 35	0.5436	$6.00^{+0.57}_{-0.62}$
PSZ2 G136.92+59.46	Abell 1436 RXC J1200.3+5613			0.0650	$1.80^{+0.17}_{-0.16}$
PSZ2 G143.26+65.24	Abell 1430 RXC J1159.2+4947 ZwCl 1156.4+5009	11 59 17	+49 47 37	0.3634	$7.65^{+0.42}_{-0.44}$
PSZ2 G144.33+62.85	Abell 1387 RXC J1149.0+5135	11 49 05	+51 35 08	0.1320	$2.66^{+0.33}_{-0.38}$
PSZ2 G145.65+59.30	Abell 1294 ZwCl 1129.6+5430	11 32 42	+54 13 12	0.3475	$4.73^{+0.59}_{-0.64}$
PSZ2 G150.56+58.32	MACS J1115.2+5320 RXC J1115.2+5320	11 15 11	+53 19 39	0.4660	$7.55^{+0.50}_{-0.52}$
PSZ2 G151.62+54.78	RX J105453.3+552102 [WH2015] 0472 1RXS J105453.3+552102	10 54 52	+55 21 13	0.4864	$5.37^{+0.68}_{-0.75}$
PSZ2 G156.26+59.64	[WH2015] 0485	11 08 30	+50 16 02	0.6175	$6.77^{+0.59}_{-0.60}$
Abell 1156		11 04 56	+47 25 15	0.2091	...
Abell 1314		11 34 49	+49 04 40	0.0335	...
Abell 1615		12 47 43	+48 51 57	0.2106	...
GMBCG J211.77332+55.09968		14 06 55	+55 04 02	0.2506	...
MaxBCG J173.04772+47.81041		11 32 11	+47 48 38	0.2261	...
NSC J143825+463744		14 38 46	+46 39 56	0.0357	...
RXC J1053.7+5452	MCXC J1053.7+5452	10 53 44	+54 52 20	0.0704	...
WHL J125836.8+440111		12 58 37	+44 01 11	0.5339	...
WHL J122418.6+490549		12 24 19	+49 05 50	0.1004	...
WHL J124143.1+490510		12 41 43	+49 05 10	0.3707	...
WHL J132226.8+464630		13 22 27	+46 46 30	0.3718	...
WHL J132615.8+485229		13 26 16	+48 52 29	0.2800	...
WHL J133936.0+484859		13 39 36	+48 48 59	0.3265	...
WHL J134746.8+475214		13 47 47	+47 52 15	0.1695	...

Table 3. Cluster radio properties.

Cluster	Classification	LLS (Mpc)	S_{144} (mJy)
PSZ2 G080.16+57.65	cHalo, Relic	(R) 1.1, (H) ∼ 1	(H) 92 ± 32, (R) 55.8 ± 11.6
PSZ2 G084.10+58.72[(a)]	cHalo	0.5	4.2 ± 1.2
PSZ2 G086.93+53.18[(a)]	Halo	0.6	12.4 ± 3.6
PSZ2 G087.39+50.92	AGN-no diffuse	–	–
PSZ2 G088.98+55.07	AGN-no diffuse	–	–
PSZ2 G089.52+62.34	(A) Relic	(A) 0.23	(A+C) 74.6 ± 15.0
	(B) cRelic (A+B: cdRelic)	(B) 0.17	(B) 12.2 ± 2.6
	D (Relic)	(D) 0.9	(D) 31.8 ± 8.2
PSZ2 G095.22+67.41	cRelic	0.4	6.8 ± 1.5
PSZ2 G096.14+56.24	AGN-no diffuse	–	–
PSZ2 G098.44+56.59	AGN-no diffuse	–	–
PSZ2 G099.86+58.45[(b)]	Halo	1.0	14.7 ± 3.2
PSZ2 G106.61+66.71	cHalo	0.5	20 ± 4
PSZ2 G107.10+65.32[(c)]	dHalo	(Hn) 2.0, (Hs) 1.3	(Hn) 123 ± 25, (Hs) 63 ± 14
	Relic (s)	0.5	20.9 ± 4.3
	cFossil (n: S1, S2)	(S1) 0.4, (S2) 0.23	(S1) 79 ± 17, (S2) 17.5 ± 3.6
PSZ2 G111.75+70.37[(d)]	Relic	0.7	(R) 106.7 ± 21.4
	Halo	∼ 0.6	27.7 ± 6.3
PSZ2 G114.31+64.89	Halo	0.5	91.7 ± 18.6
PSZ2 G114.99+70.36[(e)]	cHalo, cFossil	–	(⋆)
PSZ2 G118.34+68.79	cHalo, Fossil	(H) ∼ 0.4, (F) 0.5	(H) 28 ± 13, (F) 67 ± 13
PSZ2 G123.66+67.25	cFossil	0.26	7.5 ± 1.6
PSZ2 G133.60+69.04[(f)]	Halo, cdRelic/cFossil	(H) 0.9	(H) 129 ± 26
PSZ2 G135.17+65.43	cHalo	0.5	29.0 ± 6.6
	cRelic/cFossil	0.4	9.14 ± 1.9
PSZ2 G136.92+59.46	AGN-no diffuse	–	–
PSZ2 G143.26+65.24[(g)]	Halo	1.5	(H) 29.8 ± 6.6
PSZ2 G144.33+62.85	AGN-no diffuse	–	–
PSZ2 G145.65+59.30	cHalo/cFossil	0.4	6.7 ± 1.7
PSZ2 G150.56+58.32	Halo	1.0	71.2 ± 14.5
PSZ2 G151.62+54.78	AGN-no diffuse	–	–
PSZ2 G156.26+59.64	cHalo	0.5	7.9 ± 3.7
RXC J1053.7+5452[(h)]	Relic	0.75	214 ± 43
Abell 1156	cHalo	0.7	15.7 ± 6.8
Abell 1314[(i)]	Fossil (central)	0.44	136.9 ± 27.4
Abell 1615	AGN-no diffuse	–	–
MaxBCG J173.04772+47.81041	AGN-no diffuse	–	–
NSC J143825+463744	Unclassified	0.4	–
GMBCG J211.77332+55.09968	AGN-no diffuse	–	–
WHL J125836.8+440111	Halo	0.8	58.4 ± 11.7
WHL J122418.6+490549	Fossil	0.37	209 ± 42
WHL J124143.1+490510	cHalo	1.2	(⋆)
WHL J132226.8+464630	cHalo	0.5	(⋆)
WHL J132615.8+485229	AGN-no diffuse	0.32	(⋆)
WHL J133936.0+484859	cHalo	∼ 0.3	(⋆)
WHL J134746.8+475214	AGN-no diffuse	–	–

Notes. H = halo, R = relic, d = double, c = candidate, s = south, n = north, LLS = largest linear size. (⋆)Radio emission is blended with other sources, and therefore no reliable flux density measurement can be obtained. Literature references that first reported the presence of diffuse emission in these clusters: [(a)]Di Gennaro et al. (2021); [(b)]Cassano et al. (2019); [(c)]Kempner & Sarazin (2001) and Botteon et al. (2018); [(d)]Shimwell et al. (2019); [(e)] Venturi et al. (2008); [(f)]Govoni et al. (2012); [(g)]Hoeft et al. (2020); [(h)]Rudnick & Lemmerman (2009); [(i)]Wilber et al. (2019).

of $M_{500} = 2.51^{+0.20}_{-0.21} \times 10^{14}\, M_{\odot}$. The high-resolution radio image (see Fig. 5) shows a complex central region with several AGNs present as well as more extended emission. A low-surface-brightness arc-like structure is found about 1.3 Mpc to the east of the optical center of the cluster. This source has a largest linear size (LLS) of about 1.1 Mpc. In a low-resolution image (made with a 90″ taper), additional faint diffuse emission spanning the central region of the cluster is found. This emission extends all the way to the arc-like structure to the east. This emission has a size of approximately 1.0 Mpc by 1.8 Mpc. The XMM image reveals an E-W merging cluster whose main component is located at the optical center of the cluster. We classify the

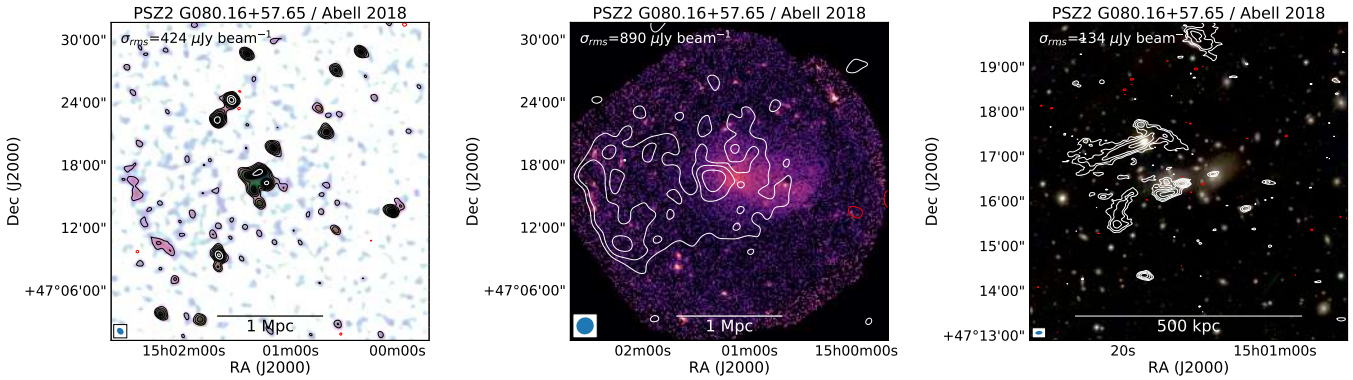

Fig. 5. PSZ2 G080.16+57.65, Abell 2018. *Left*: low-resolution 144 MHz radio image made with a 30″ taper. *Middle*: *XMM-Newton* image with radio contours from a 90″ tapered image overlaid. Compact sources were subtracted in this image. *Right*: Pan-STARRS *gri* color image overlaid with radio contours from the robust −0.5 weighted image. The cluster center position is marked with a white "X". Radio contours are drawn at $3\sigma_{\rm rms} \times [1, 2, 4, \ldots]$, where $\sigma_{\rm rms}$ is the rms map noise. Negative $-3\sigma_{\rm rms}$ contours are drawn in red. The rms noise levels of the radio images used are provided in the top right corner of each panel.

arc-like structure to the east as a giant radio relic and the large-scale centrally placed emission as a candidate radio halo. The nature of the central brighter diffuse emission near the AGNs remains unclear. It could be related to the radio halo or be revived fossil plasma from the AGNs. For the candidate radio halo we determined an integrated flux density of $S_{144} = 92 \pm 32$ mJy by masking the central brighter diffuse emission around the AGNs and the extension toward the radio relic in the fitting. We note that this cluster falls above the correlation between cluster mass and radio power (see Sect. 5.2). Deeper observations are required to shed more light on this point and on the origin of the extension from the central emission toward the relic.

4.2. PSZ2 G089.52+62.34, Abell 1904

The *XMM-Newton* image reveals a disturbed cluster, with the ICM being elongated in the NE-SW direction (see Fig. 6). In the LOFAR image we detect two arc-like radio sources to the north (source A) and SE (source B) of the cluster center. At the redshift of the cluster ($z = 0.0701$), these sources have an LLS of 230 and 170 kpc, respectively. Sources A and B are located at projected distances to the cluster center of 350 and 150 kpc, respectively. Despite these relatively small distances, we consider these sources to be peripheral given the ICM distribution. A much fainter elongated source (C) is visible NW of source A. No optical counterparts are detected for these sources. A compact double-lobed radio galaxy is located just west of source A. Given the peripheral location of source A with respect to the ICM distribution and elongated ICM shape, we classify source A as a radio relic. The location of source B is somewhat peculiar with respect to the overall ICM elongation. Given that source B is also affected by calibration artifacts from a nearby bright source, we classify it as a candidate radio relic. Assuming the classification of source B is confirmed, this cluster hosts a double radio relic in combination with relic A. The A and B (candidate) relics in Abell 1904 are relatively small compared to other well-studied relics, although we note that, for example, the western relic in ZwCl 0008.8+5215 also has a small LLS of 290 kpc (Di Gennaro et al. 2019).

In our images an additional elongated source (D) is visible 1.6 Mpc to the NE of the cluster center (see Fig. 6, top right panel). The source has no optical counterpart and a relatively sharp outer boundary, while the emission fades more slowly in the direction of the cluster center. Given its LLS of 0.9 Mpc and location along the merger axis, as indicated from the X-ray image, we classify this source as another radio relic.

4.3. PSZ2 G095.22+67.41, RXC J1351.7+4622

PSZ2 G095.22+67.41 is a relatively nearby cluster located at $z = 0.0625$. The *XMM-Newton* image reveals that the ICM peak coincides with the location of the BCG (see Fig. 7). A faint X-ray extension is visible to the east. This suggests that the cluster is not fully relaxed and is undergoing a merger event in the E-W direction.

No central diffuse radio emission is found in our LOFAR image. However, we detect a N-S elongated source about 0.8 Mpc to the east of the cluster center. The source has an LLS of about 0.4 Mpc and is located south of a brighter radio galaxy. We classify the source as a relic that is tracing a shock that could have originated from the E-W merger event. This is consistent with the N-S positioning, highly elongated shape, and peripheral location of the radio source. An alternative explanation is that this source traces (old) AGN plasma from a bright elliptical galaxy (MCG+08-25-051, $z = 0.0623$) that is located near this source. A faint (∼0.5 mJy) compact radio counterpart is detected in our LOFAR image for MCG+08-25-051. However, there is no evidence of jets or lobes originating from this source, which therefore suggests that the emission resulted from a previous episode of AGN activity.

4.4. PSZ2 G106.61+66.71

The LOFAR image displays two bright, partly blended tailed radio galaxies in the western part of the cluster (see Fig. 8). The *Chandra* X-ray image shows a cluster without a strongly peaked core. In addition, the cluster is elongated in the direction of the two tailed radio galaxies. In the center of the cluster we detect diffuse radio emission with an LLS of about 0.5 Mpc. Within this diffuse emission we find two compact AGNs associated with the cluster, including the BCG. We consider a mini-halo origin unlikely given the lack of centrally peaked X-ray emission. The western part of the central diffuse emission has a rather high surface brightness, suggesting a link with a cluster AGN. On the other hand, some of the emission (in particular the eastern part) has a smooth morphology somewhat similar to a radio halo. For the above reasons we list the source as a candidate radio halo.

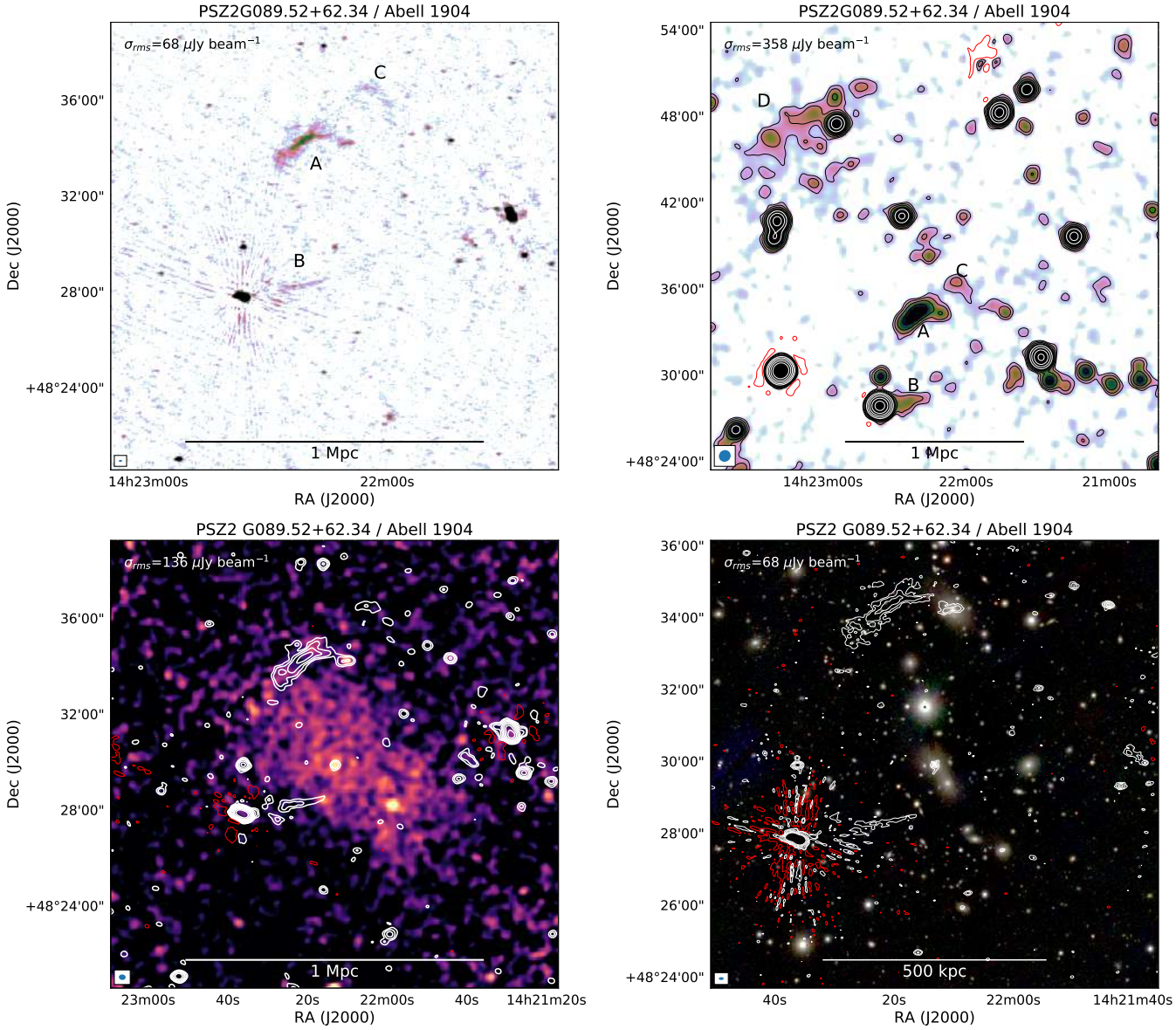

Fig. 6. PSZ2 G089.52+62.34, Abell 1904. *Top left*: robust −0.5 radio image. *Top right*: 30″ tapered radio image. *Bottom left*: *XMM-Newton* X-ray image with 10″ tapered radio contours. *Bottom right*: optical image with robust −0.5 image radio contours. For more details, see the caption of Fig. 5.

4.5. PSZ2 G111.75+70.37, Abell 1697

The *XMM-Newton* X-ray image shows an elongated cluster without a central concentration. The LOFAR images reveal two prominent radio sources in this cluster (see Fig. 9). One is located near the SW BCG of the cluster. The second source is more extended and located at the NE periphery of the cluster. This emission is also discussed by Paul et al. (2020) based on LoTSS DR1 images (Shimwell et al. 2019). The source consists of a NW-SE elongated structure with an LLS of about 700 kpc, as well as emission trailing SW toward a second BCG. Compact radio emission from this BCG is detected, but no obvious morphological connection with the extended source is visible. The extended source somewhat resembles the Toothbrush relic (van Weeren et al. 2012). We note that the extended radio source partly overlaps with the nearby irregular dwarf galaxy UGC 8308 (DDO 167; e.g., Tikhonov & Karachentsev 1998). However, we consider an association of the radio source with the cluster more likely. We therefore classify the source as a radio relic. This classification is also consistent with the elongation of the ICM, suggesting a NE-SW merger event. In the low-resolution radio images, extended emission is visible in the region between the NE and the SW BCGs. This emission is classified as a radio halo since it follows the X-ray emission from the ICM. The flux density of the halo is 27.7 ± 6.3 mJy. We note that this emission is also discussed by Paul et al. (2020, "trailing relic emission"), who concluded that this emission has an ultra-steep spectrum. We note, however, that the flux density estimate provided by Paul et al. (2020) is incorrect as the emission is not fully deconvolved in the LoTSS DR1 images, and thus measurements made directly from those images are complicated. This leads to a large overestimation of the flux density, as discussed by Shimwell et al. (2019). This problem is addressed to some extent in the upcoming DR2.

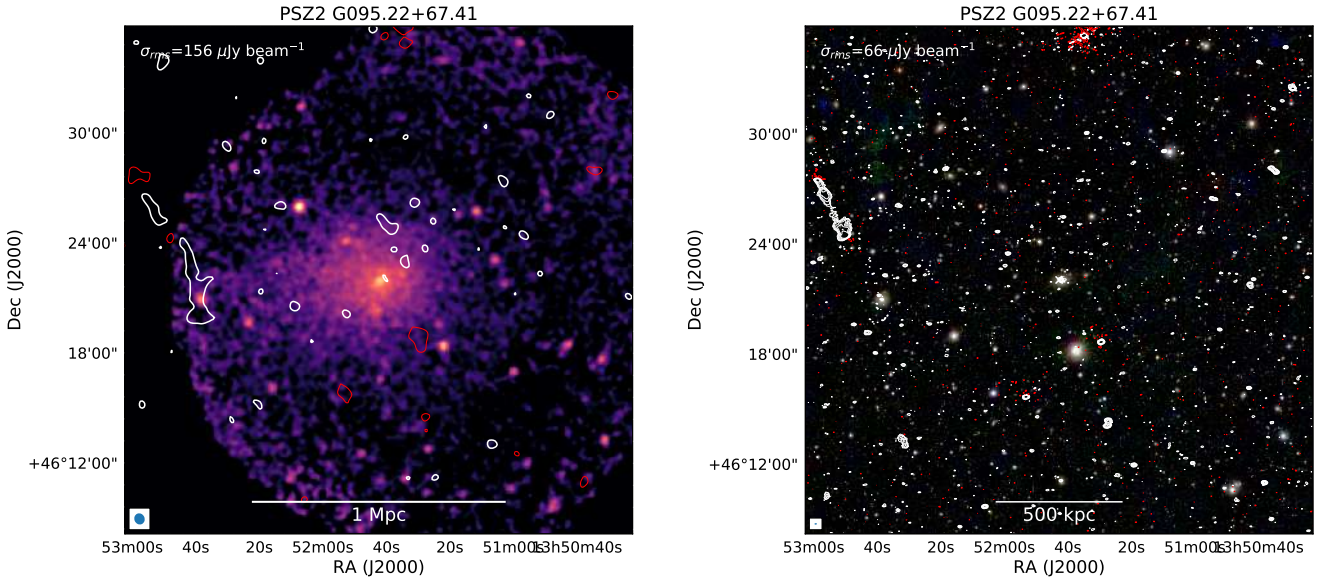

Fig. 7. PSZ2 G095.22+67.41, RXC J1351.7+4622. *Left*: *XMM-Newton* X-ray image with 30″ tapered radio contours (compact sources were removed). *Right*: optical image with robust −0.5 image radio contours. For more details, see the caption of Fig. 5.

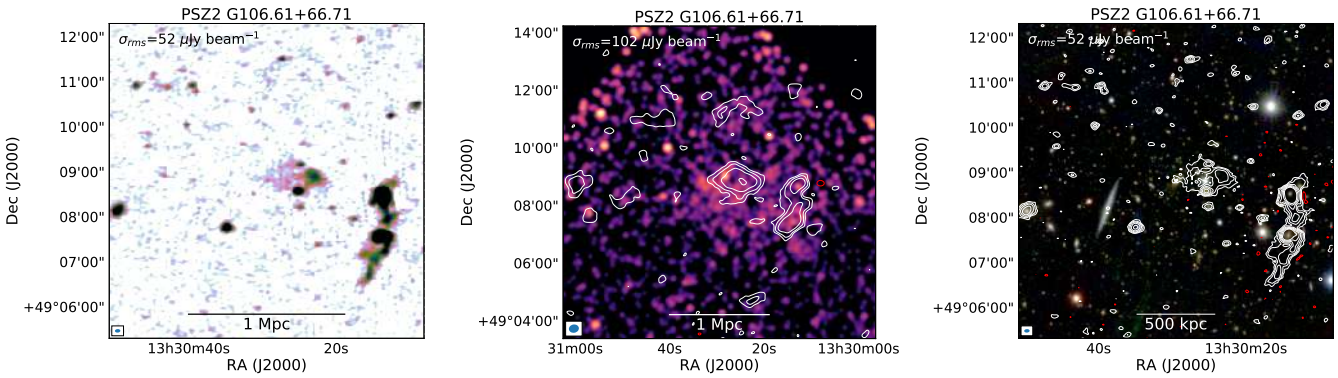

Fig. 8. PSZ2 G106.61+66.71. *Left*: robust −0.5 radio image. *Middle*: *Chandra* X-ray image with 10″ tapered radio contours (compact sources were subtracted). *Right*: optical image with robust −0.5 image radio contours. For more details, see the caption of Fig. 5.

4.6. PSZ2 G114.31+64.89, Abell 1703

The massive cluster Abell 1703 has been extensively studied at optical wavelengths due to its gravitational lensing properties. It is generally classified as a relaxed cluster (e.g., Umetsu et al. 2011; Richard et al. 2009). The *Chandra* image shows an overall regular appearance, with the cluster being somewhat elongated in the NNW-SSE direction (see Fig. 10). Andrade-Santos et al. (2017) determined the concentration parameters, "cuspiness," and central density of the cluster using *Chandra* X-ray data. These properties, however, point to a non-cool core classification. Furthermore, a recent dynamical analysis from Boschin et al. (2020) indicates that this is a merging cluster that consists of two or three sub-clumps.

The LOFAR image reveals the presence of central diffuse emission, filling the region between tailed radio source A and a complex compact region of emission that we labeled B. Source B is likely related to AGN activity. A faint tailed source, labeled C, is located in the SE part of the cluster. The total extent of the diffuse emission is difficult to determine because of sources A and B. Given the central location and extent of at least 0.5 Mpc, we classify the diffuse emission as a radio halo with an integrated flux density of 91.7 ± 18.6 mJy based on an elliptical model fit.

4.7. PSZ2 G118.34+68.79

Several radio galaxies and diffuse emission are detected in this cluster (see Fig. 11). An optical image shows two BCGs that are located along a SE-NW axis. The cluster hosts a tailed radio galaxy, labeled A. To the east, a bright patch of emission (B) is found just above the SE BCG. Additional fainter emission is located around B. Given the high surface brightness of B and several nearby radio AGNs, B is likely AGN plasma, possibly revived by the passage of a shock.

We also find low-level diffuse emission extending on scales of about 0.4 Mpc in the central regions of the cluster, labeled H. However, it is hard to determine its full spatial extent as it partly blends with other extended radio sources in this region. Since the diffuse emission approximately follows the overall galaxy distribution and has a low surface brightness, we classify it as a candidate radio halo. Fitting a circular model, we estimate S_{144} = 28 ± 13 mJy, where we masked the region near B and west of A.

4.8. PSZ2 G133.60+69.04, Abell 1550

The existence of diffuse emission in the Abell 1550 cluster (z = 0.2540) was first reported by Govoni et al. (2012). Extended

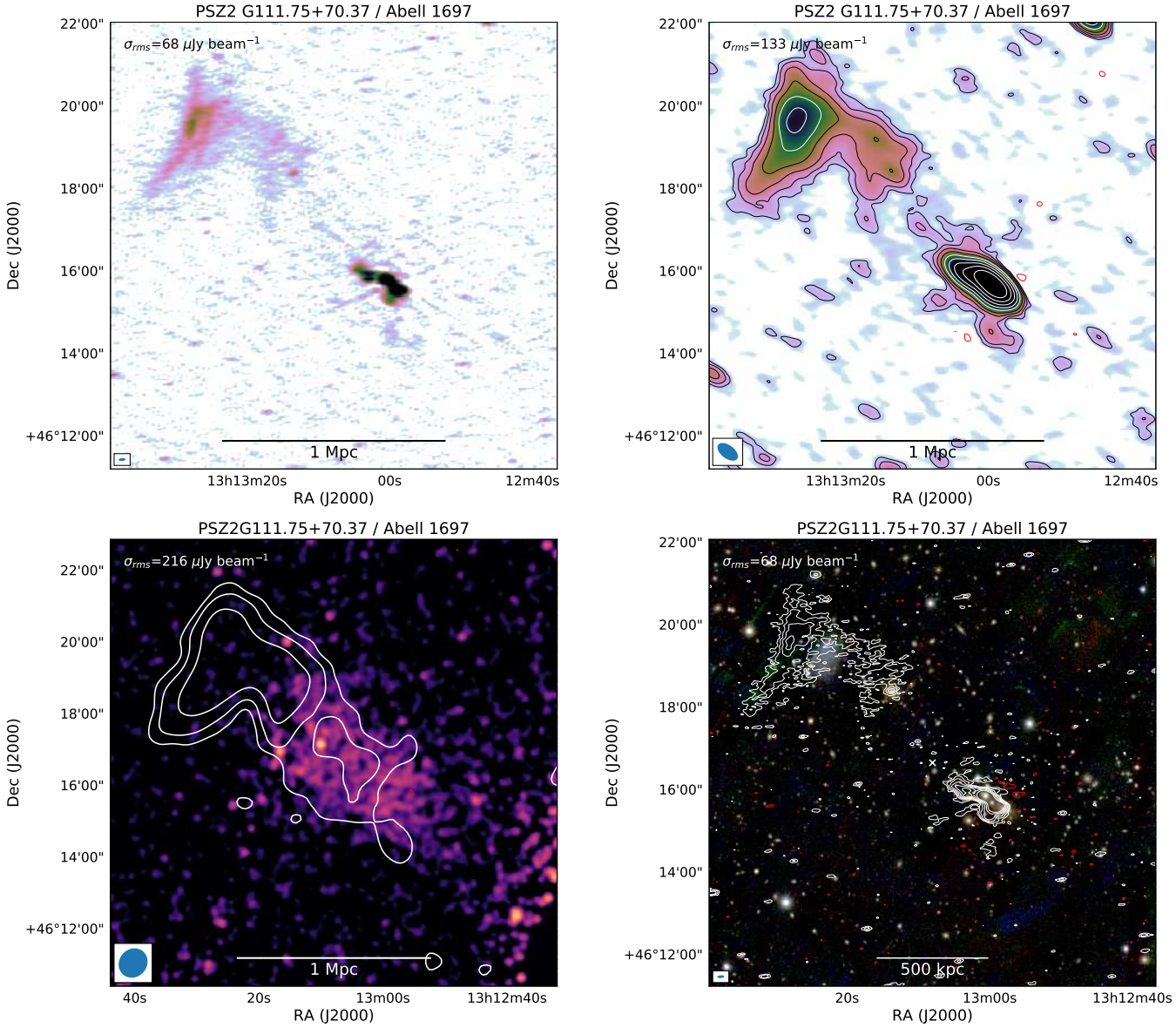

Fig. 9. PSZ2 G111.75+70.37, Abell 1697. *Top left*: robust −0.5 radio image. *Top right*: 10″ tapered radio image. *Bottom left*: *XMM-Newton* X-ray image with 30″ tapered radio contours (compact sources were subtracted). *Bottom right*: optical image with robust −0.5 image radio contours. For more details, see the caption of Fig. 5.

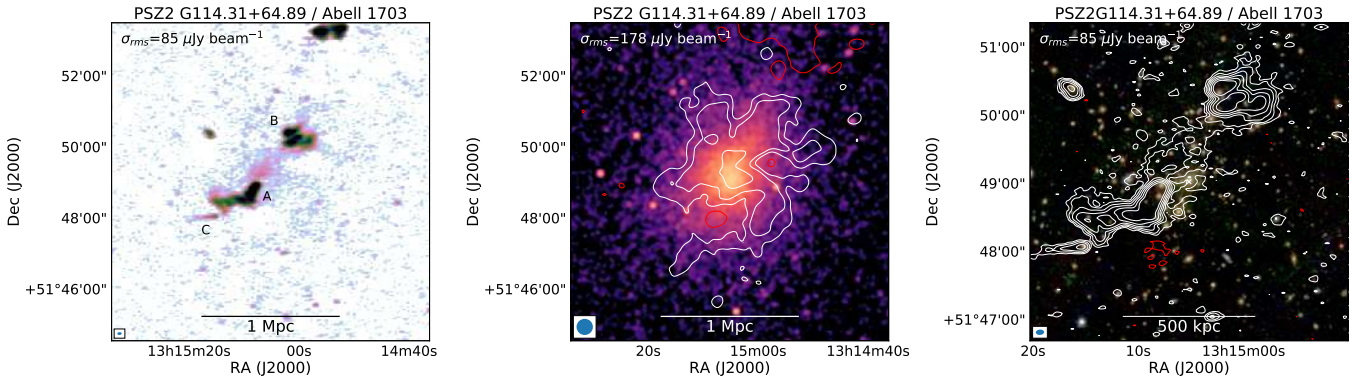

Fig. 10. PSZ2 G114.31+64.89, Abell 1703. *Left*: robust −0.5 radio image. *Middle*: *Chandra* X-ray image with 15″ tapered radio contours (compact sources were subtracted). *Right*: optical image with robust −0.5 image radio contours. For more details, see the caption of Fig. 5.

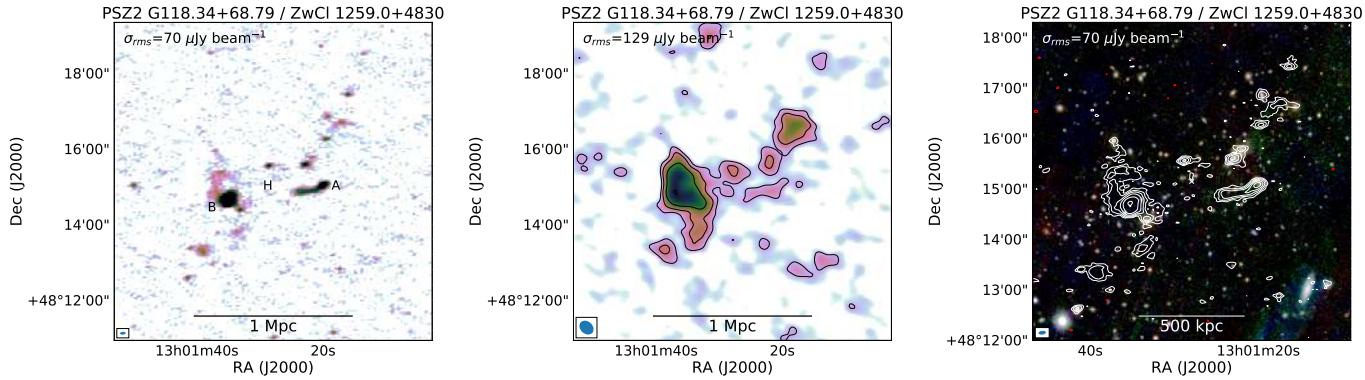

Fig. 11. PSZ2 G118.34+68.79. *Left*: robust −0.5 radio image. *Middle*: 15″ tapered radio image with compact radio sources subtracted. *Right*: optical image with robust −0.5 image radio contours. For more details, see the caption of Fig. 5.

radio emission is clearly detected in this cluster by LOFAR (see Fig. 12). It extends over a significantly larger region than found by Govoni et al. (2012), corresponding to an LLS of 1.8 Mpc. This is explained by the shallower depth of the Very Large Array (VLA) image used by Govoni et al. (2012) and/or a steep radio spectrum.

The *Chandra* image shows a roughly roundish ICM distribution. Additional faint X-ray emission is observed NE of the main structure. The main part of the diffuse radio emission, labeled H, traces the X-ray emission from the ICM. We therefore classify it as a giant radio halo with a size of about 0.9 Mpc. Based on the elliptical model fit, we obtain a radio halo integrated flux density of 129 ± 26 mJy. The radio images also show a bright tailed radio galaxy (A) and several structures in the western part of the cluster (D, E, and C) that do not have clear optical counterparts. A diffuse patch of emission, labeled B, is placed near a group of galaxies located at the same redshift as the main cluster. A lower-resolution radio image shows that B is connected to the main radio halo. Source B seems to be associated with the NE X-ray extension. Sources E, D, and C look to be relics, possibly related to revived AGN fossil plasma. We note that both D and C are connected to the emission from the main radio halo. Based on the extension of the ICM and the placement of the diffuse radio sources, the cluster seems to have undergone a merger event in the NE-SW direction. The location of B in the NE and the locations of C, D, and E in the SW could indicate that these structures are related to mergers shocks. If this interpretation is correct, the cluster hosts a double radio relic. The combination of a double radio relic and a radio halo is relatively rare (Bonafede et al. 2017).

4.9. PSZ2 G135.17+65.43

The LOFAR image uncovers a large number of radio galaxies in this $z = 0.5436$ cluster, which are labeled A to F (see Fig. 13). One of these, source E, has a physical extent of about 1 Mpc, and we classify it as a giant double-double. Sources A to D display head-tail morphologies. Source G is a peripheral source with an extent of about 400 kpc. We do not identify an optical counterpart for this source and tentatively classify it as a relic or an AGN fossil plasma source. The *Chandra* image of PSZ2 G135.17+65.43 indicates a non-relaxed cluster without a clear central peak. We also detect central diffuse emission in this cluster with a total extent of about 500 kpc, labeled H. Due to the presence of tailed radio galaxies A and B, the full extent of H is hard to determine, but the emission approximately follows the thermal ICM. Given its central location and extent, we classify H as a candidate radio halo with a flux density of $S_{144} = 29.0 \pm 6.6$ mJy based on the circular model fit.

4.10. PSZ2 G145.65+59.30, Abell 1294

An *XMM-Newton* image shows a cluster that is elongated in the E-W direction (see Fig. 14). The galaxy distribution shows a similar elongation, extending all the way to a tailed radio galaxy (A). Our LOFAR image reveals faint diffuse emission, with an LLS of about 0.4 Mpc, located in the western part of the cluster. This emission is very faint and close to the detection limit of our observations. A candidate tailed radio galaxy (B) is located just east of the diffuse radio source. The diffuse emission is difficult to classify with the current data at hand. One possibility is that it is related to revived or reaccelerated fossil plasma from source B. Alternatively, it could also be a radio halo, somewhat similar to the "off-axis" radio halo found in Abell 1132 (Wilber et al. 2018). The integrated flux density of the diffuse source is $S_{144} = 6.7 \pm 1.7$ mJy, based on the circular model fit.

4.11. PSZ2 G150.56+58.32, MACS J1115.2+5320

MACS J1115.2+5320 is a massive merging cluster located at $z = 0.466$. A *Chandra* X-ray image reveals an ongoing merger event along a NW-SE axis (see Fig. 15). Mann & Ebeling (2012) classified this system as a possible head-on binary cluster merger. The global temperature of the cluster was measured to be 8.6 ± 1.1 keV by Morandi et al. (2015).

The LOFAR image shows a long 770 kpc tailed radio galaxy (A), with the tail pointing toward the NW. Two additional tailed radio galaxies (B and C) have their tails pointing toward the SE. Source D is located just SE of the head-tail source (A) and has a rather complex morphology in our high-resolution image. Near source D, a possible merger-induced cold front is visible in the *Chandra* image. Low-surface-brightness radio emission is detected in the region north of source A. This emission extends over 1 Mpc, and, given its size, we classify it as a giant radio halo. Fitting an elliptical model, we determine $S_{144} = 71.2 \pm 14.5$ mJy for the radio halo.

4.12. PSZ2 G156.26+59.64

A bright compact radio source is detected in this $z = 0.6175$ cluster, which seems to be associated with a BCG (see Fig. 16). In our low-resolution images, with compact sources removed,

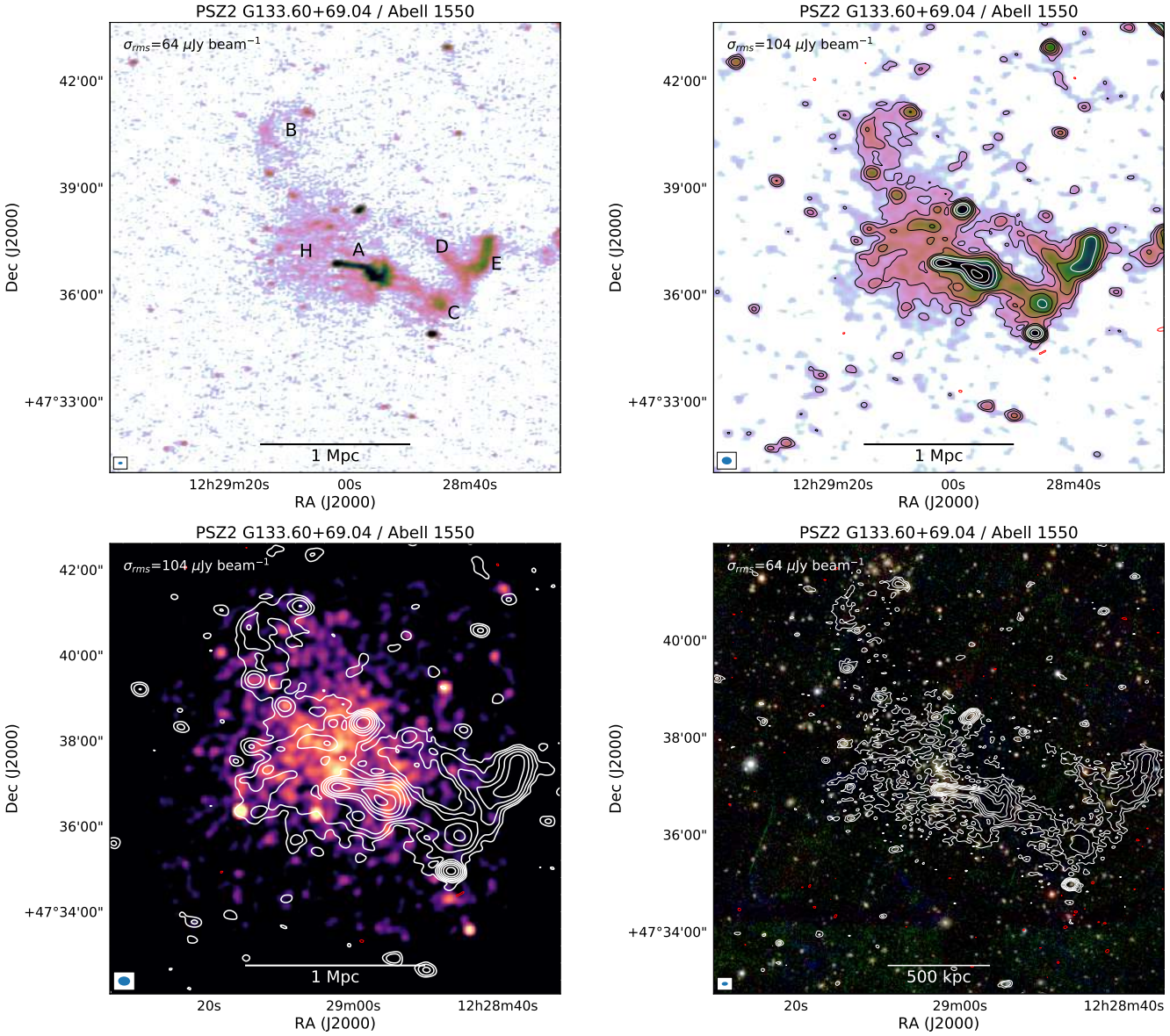

Fig. 12. PSZ2 G133.60+69.04, Abell 1550. *Top left*: robust −0.5 radio image. *Top right*: 10″ tapered radio image. *Bottom left*: *Chandra* X-ray image with 10″ tapered radio contours. *Bottom right*: optical image with Robust −0.5 image radio contours. For more details, see the caption of Fig. 5.

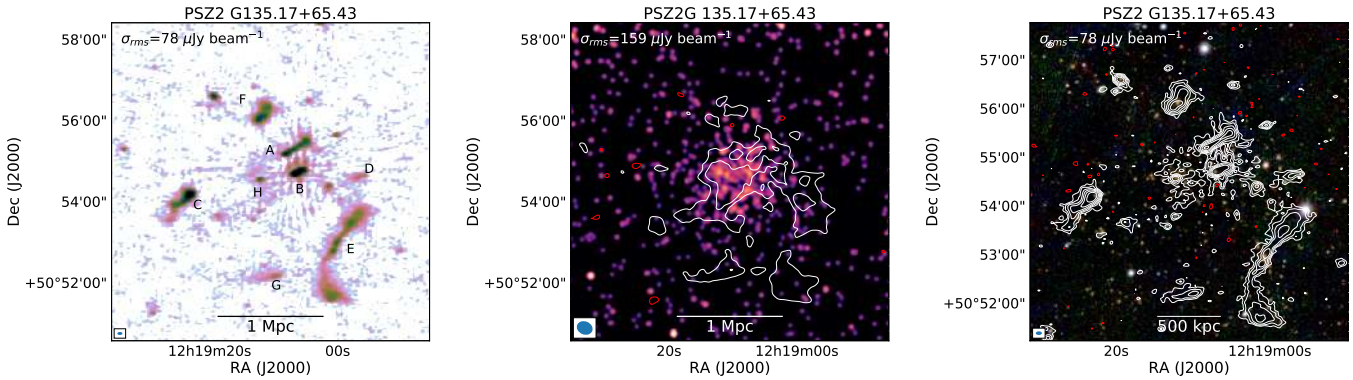

Fig. 13. PSZ2 G135.17+65.43. *Left*: robust −0.5 radio image. *Middle*: *Chandra* X-ray image with 10″ tapered radio contours (compact sources were subtracted). *Right*: optical image with robust −0.5 image radio contours. For more details, see the caption of Fig. 5.

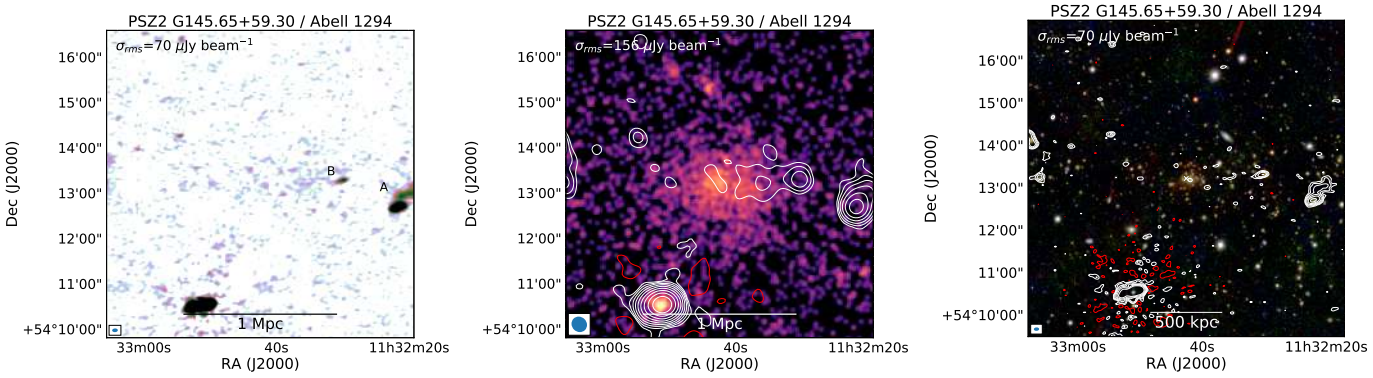

Fig. 14. PSZ2 G145.65+59.30, Abell 1294. *Left*: robust −0.5 radio image. *Middle*: *XMM-Newton* X-ray image with 10″ tapered radio contours. *Right*: optical image with robust −0.5 image radio contours. For more details, see the caption of Fig. 5.

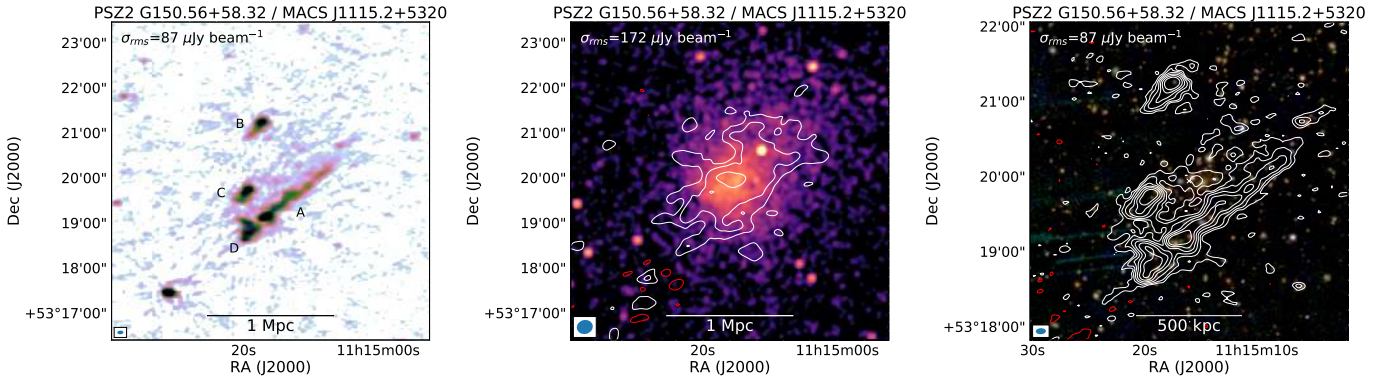

Fig. 15. PSZ2 G150.56+58.32, MACS J1115.2+5320. *Left*: robust −0.5 radio image. *Middle*: *Chandra* X-ray image with 10″ tapered radio contours (compact sources were subtracted). *Right*: optical image with robust −0.5 image radio contours. For more details, see the caption of Fig. 5.

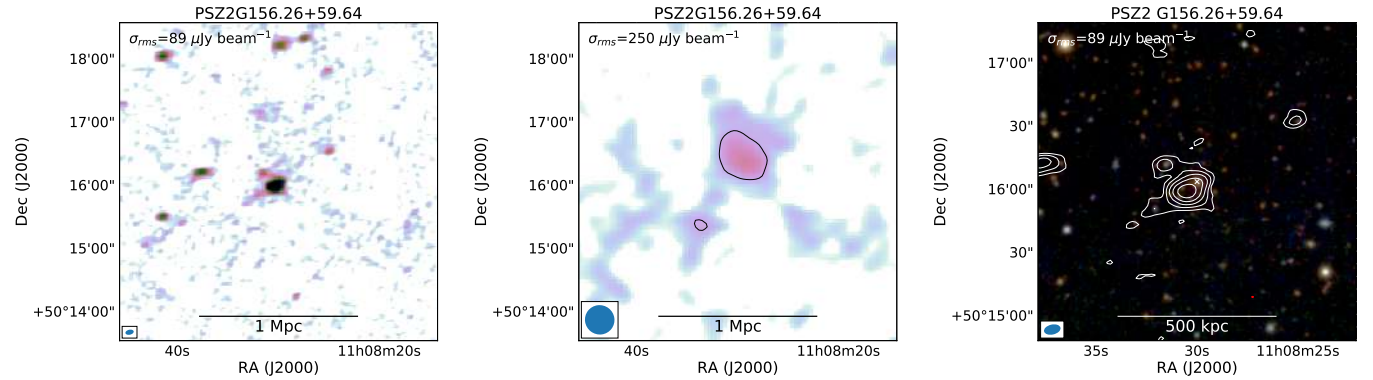

Fig. 16. PSZ2 G156.26+59.64. *Left*: robust −0.5 radio image. *Middle*: 15″ tapered radio image with compact sources subtracted. *Right*: optical image with robust −0.5 image radio contours. For more details, see the caption of Fig. 5.

faint diffuse emission is detected in the region above the compact radio source. Only a hint of this emission is detected in our high-resolution image. This diffuse emission has a total extent of about 0.5 Mpc. Given its approximate central location (with respect to the cluster member galaxies as judged from the Pan-STARRS images) and large physical size, we classify this source as a candidate radio halo. For the source we determine a flux density of 7.9 ± 3.7 mJy.

4.13. Abell 1156

A *Chandra* X-ray image displays a cluster that is elongated in the N-S direction (Fig. 17). Diffuse radio emission, also elongated in the N-S direction, is detected in this cluster with an LLS of 0.7 Mpc. This radio emission does not peak at the cluster center, but rather south of it. However, some faint diffuse emission is also visible north of the cluster center. We list this source as a candidate radio halo that originated from a possible N-S merger event. Additional extended radio emission, with a mostly E-W elongation, is found in the southern periphery of the cluster; its origin is not fully clear, but it might be related to AGN activity as a connection to a cluster member galaxy is suggested. The cluster also hosts a prominent head-tail radio source in the north, with the tail extending southward along the direction of the proposed merger axis. By fitting the elliptical model, we determine S_{144} = 15.7 ± 6.8 mJy for the candidate radio halo.

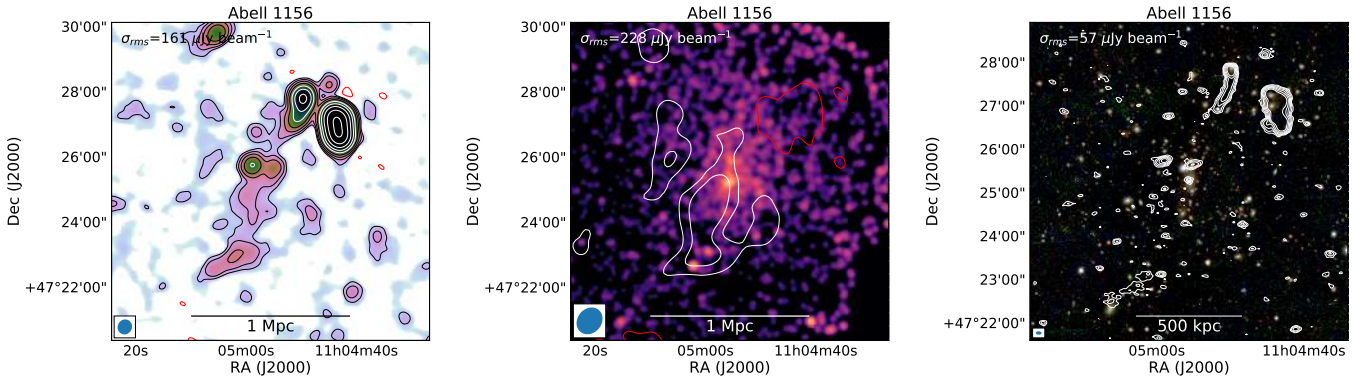

Fig. 17. Abell 1156. *Left*: 15″ tapered radio image. *Middle*: *Chandra* X-ray image with 30″ tapered radio contours (compact sources were subtracted). *Right*: optical image with robust −0.5 image radio contours. For more details, see the caption of Fig. 5.

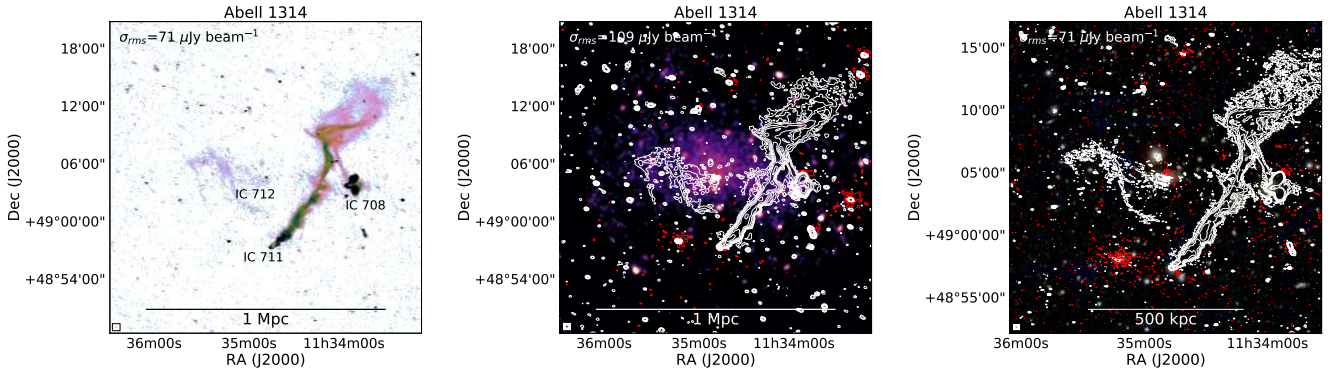

Fig. 18. Abell 1314. *Left*: robust −0.5 radio image. *Middle*: *XMM-Newton* X-ray image with 10″ tapered radio contours. *Right*: optical image with robust −0.5 image radio contours. For more details, see the caption of Fig. 5.

4.14. Abell 1314

This nearby low-mass cluster hosts a bright 800 kpc long tailed radio galaxy associated with the galaxy IC 711. The main tail shows a range of complicated linear features (see Fig. 18). LOFAR observations of this source are described in Wilber et al. (2019). Giant Metrewave Radio Telescope (GMRT) observations have been presented by Srivastava & Singal (2020) and Sebastian et al. (2017). Another smaller bright tailed radio galaxy is associated with IC 708. In addition, a filamentary source is detected near the cluster center. This is a candidate radio phoenix related to the central BCG IC 712. Our new LOFAR images of Abell 1314 reveal some additional details not visible in the previous LOFAR images presented in Wilber et al. (2019) thanks to the improved calibration. One of them is a thin elongated structure that connects IC 708 to IC 711. Its origin is unclear. In addition, our images show more clearly the filamentary nature of the phoenix source, with an LLS of 0.44 Mpc.

4.15. NSC J143825+463744

The LOFAR observations for NSC J143825+463744, a nearby $z = 0.03586$ system, are affected by bad ionospheric conditions. Despite the poor image quality, central extended emission is detected with a size of about ∼0.4 Mpc (see Fig. 19). NSC J143825+463744 was classified as a galaxy group (MLCG 1495) by Gal et al. (2003). It is composed of two dominant galaxies, NGC 5722 and NGC 5717. No X-ray emission is detected from this system by ROSAT, confirming that it has a low mass. Given the lack of an ICM detection by ROSAT, the low mass of the system, and the poor calibration, we list it as unclassified.

We note that a small E-W extended source, to the right of the image center, is associated with NGC 5714. NGC 5714 is foreground galaxy and unrelated to MLCG 1495.

4.16. WHL J122418.6+490549

WHL J122418.6+490549 hosts a bright elongated radio source with an LLS of 370 kpc (Fig. 20). This radio emission could have originated from the BCG (LEDA 2333420), which is located at the SE tip of the elongated source. The cluster is just barely detected in a *Chandra* observation, indicating a low-mass system. The source seems somewhat similar to the revived remnant radio lobe found in low-mass cluster Abell 1931 (Brüggen et al. 2018).

4.17. WHL J124143.1+490510

Faint patchy extended emission is detected in our low-resolution images of this cluster (see Fig. 21). This emission extends over a region of 1.2 Mpc. Given that the emission is approximately centered on the galaxy distribution, we classify it as a candidate radio halo.

4.18. WHL J132226.8+464630

Patchy diffuse radio emission with an extent of about 0.5 Mpc is detected west of the BCG (Fig. 22). Given its approximate central location, we classify it as a candidate radio halo.

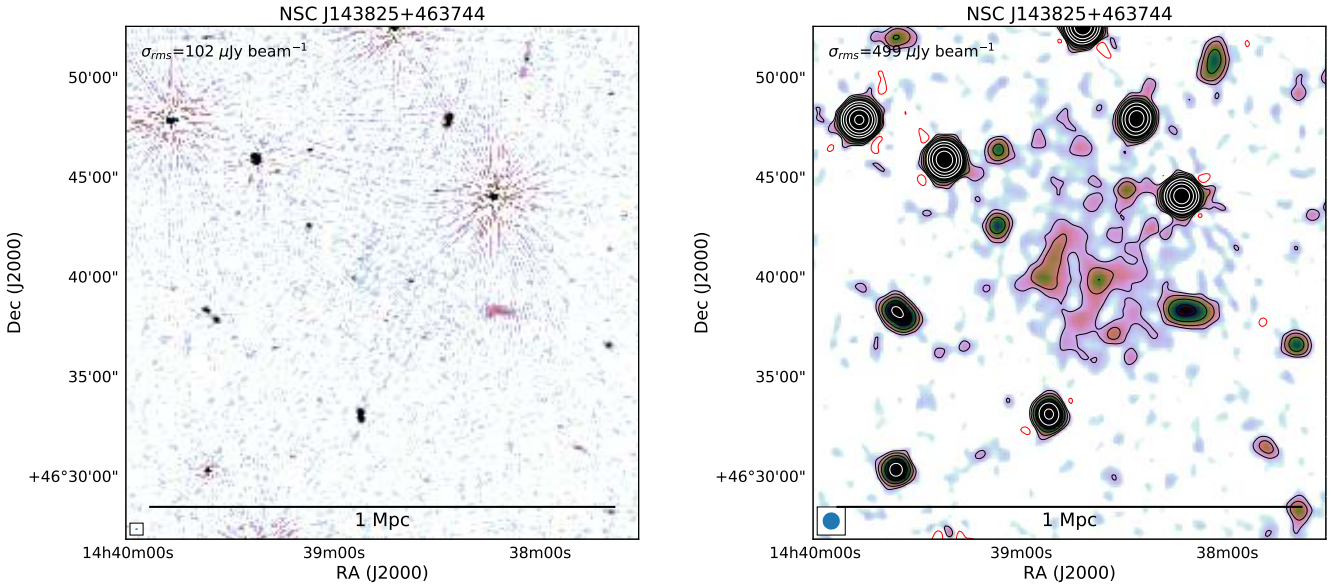

Fig. 19. NSC J143825+463744. *Left*: robust −0.5 radio image. *Right*: 30″ tapered radio image. For more details, see the caption of Fig. 5.

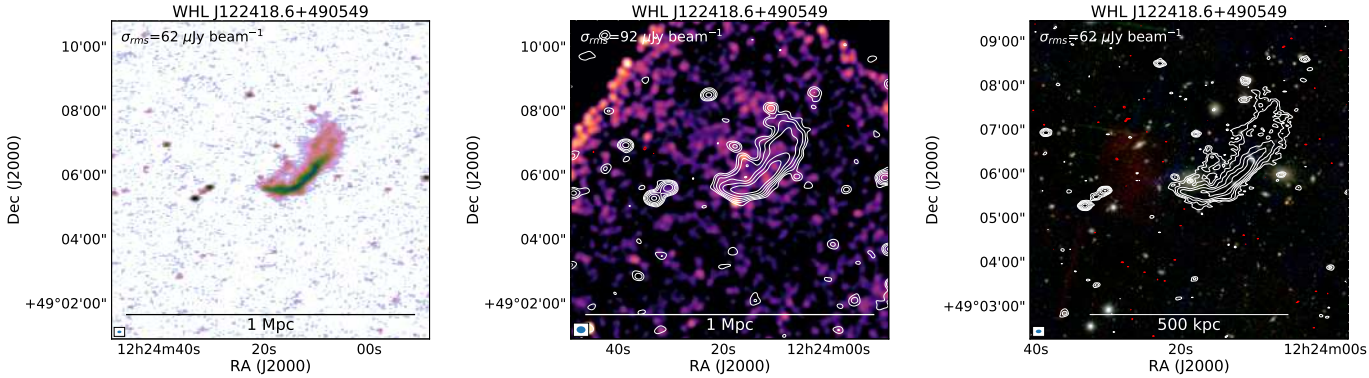

Fig. 20. WHL J122418.6+490549. *Left*: robust −0.5 radio image. *Middle*: *Chandra* X-ray image with 10″ tapered radio contours. *Right*: optical image with robust −0.5 image radio contours. For more details, see the caption of Fig. 5.

4.19. WHL J133936.0+484859

Extended radio emission is detected in this cluster, south of the BCG (see Fig. 23). This emission seems to be the extension of a tailed radio galaxy. Additional extended emission (∼300 kpc) surrounds the BCG. This candidate radio (mini-)halo will need to be confirmed with deeper observations.

4.20. WHL J125836.8+440111

In WHL J125836.8+440111 we find extended radio emission with an LLS of 800 kpc (see Fig. 24). The northern part of the emission seems to originate from two radio galaxies. However, the emission extends further south, all the way to a distorted double-lobed source. Given the large area that is covered by the extended emission, we classify part of this emission as a radio halo.

5. Discussion

5.1. Projections for the completed LoTSS survey

Based on the number of detected radio halos and relics in the HETDEX area, we can make a prediction for the number of radio halos and relics that will be detected in the completed LoTSS survey. We assume here that the LoTSS survey will have uniform sensitivity over the entire northern sky. We ignore any complications due to differences in the mass and redshift distributions between the PSZ2 clusters in the HETDEX DR1 area in the completed LoTSS survey. The uncertainties are computed based on Poisson statistics.

We first focus on the radio halos in the *Planck* PSZ2 clusters. We detect a total of eight radio halos and eight candidate halos in this sample of 26 clusters (we count PSZ2 G107.10+65.32, which consists of Abell 1758N and Abell 1758S, only once). The number of PSZ2 clusters without any diffuse emission is seven. We should note that for three of these clusters the noise levels were higher because of bad ionospheric conditions. Four PSZ2 clusters host radio relics. The fraction of confirmed radio halos in PSZ2 clusters is 31 ± 11%. Considering that there are 595 PSZ2 clusters above a declination of 0 degrees with confirmed redshifts, we estimate that there will be 183 ± 65 radio halos detected in the LoTSS survey in PSZ2 clusters. Including candidate radio halos as well, the detection fraction is 62 ± 15%. The number of PSZ2 halos in the LoTSS survey then becomes 366 ± 92. The fraction of clusters with some form of diffuse emission is 73 ± 17%. This suggests that 435 ± 99 PSZ2

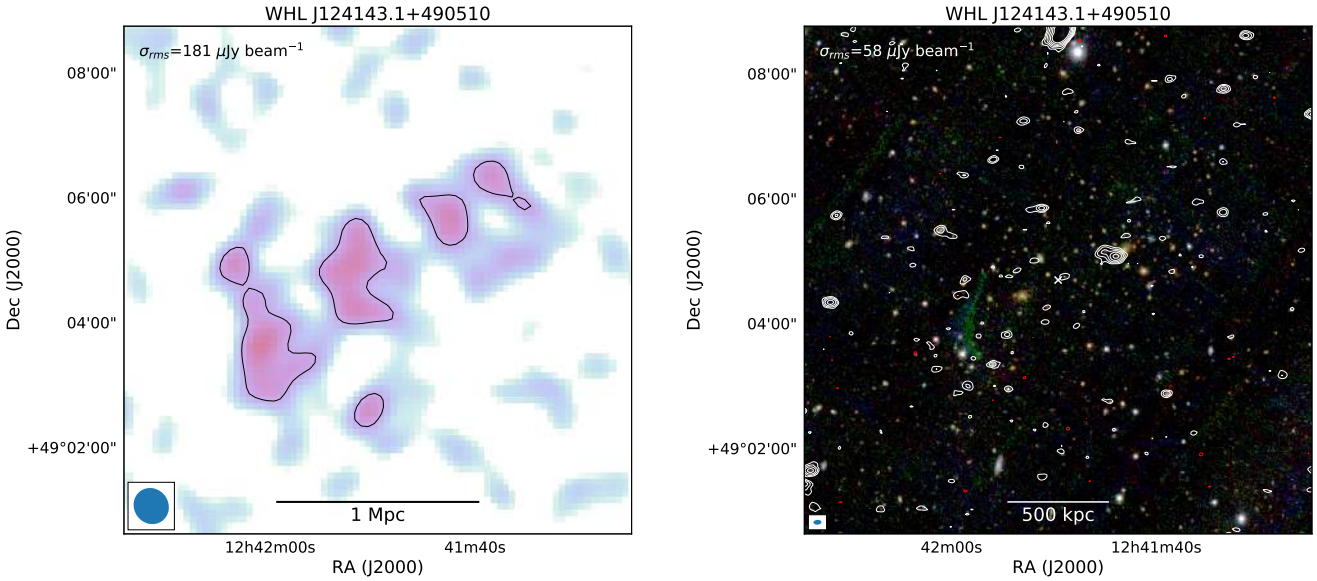

Fig. 21. WHL J124143.1+490510. *Left*: 30″ tapered radio image with compact sources subtracted. *Right*: optical image with robust −0.5 image radio contours. For more details, see the caption of Fig. 5.

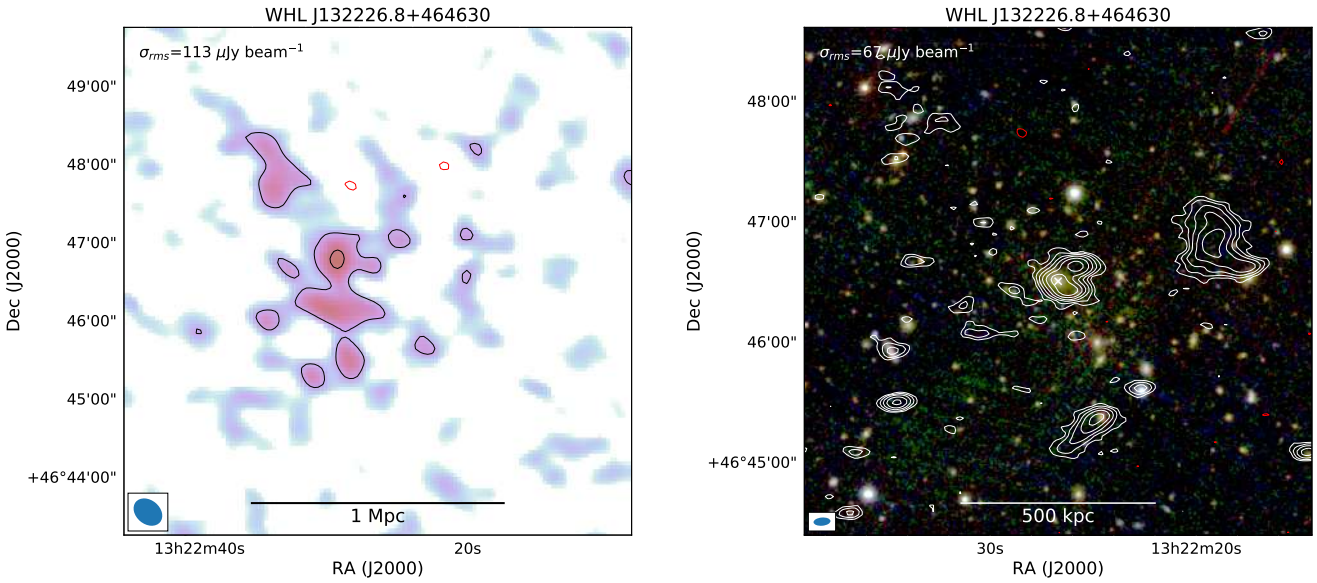

Fig. 22. WHL J132226.8+464630. *Left*: 15″ tapered radio image with compact sources subtracted. *Right*: optical image with robust −0.5 image radio contours. For more details, see the caption of Fig. 5.

clusters with diffuse emission will be detected in LoTSS. More than three-quarters of these should be new discoveries. Our LOFAR observations highlight the challenge of classifying diffuse cluster radio sources in sensitive low-frequency images. In particular, the distinction between diffuse sources and AGN fossil radio plasma is not always clear. Therefore, spectral measurements and a comparison with the thermal ICM properties will be important to correctly classify these diffuse sources.

We detect one radio halo in the non-PSZ2 clusters and four candidate radio halos. Considering these numbers, and that the region we surveyed covers 424 deg^2, we expect to find at least 10^2 radio halos in non-PSZ2 clusters in the full LoTSS. Here we have assumed that about half of the candidate radio halos are real. The total number of radio halos (PSZ2 plus non-PSZ2) that will be found in the full LoTSS survey will thus be around 400–500, again assuming that half of the candidates are real.

The number of radio halos that our extrapolation predicts for the LoTSS survey agrees with the number predicted by reacceleration models (Cassano et al. 2010a, 2012). These models predict that a significant fraction of halos have steep spectra, especially in clusters with smaller masses and higher redshifts, and that the occurrence of halos in clusters declines with cluster mass. The large amount of statistics that are expected from LoTSS will allow us to test the dependence of the occurrence of radio halos on cluster mass and redshift.

Interestingly, we did not detect clear examples of radio mini-halos. Radio mini-halos are more difficult to classify due to their smaller sizes, and the sample studied here is not known to host any strong cool-core clusters. Therefore, the lack of radio mini-halos might be (partly) related to the properties of our sample. However, there is no consensus that SZ-selected samples are biased against cool-core clusters (Eckert et al. 2011;

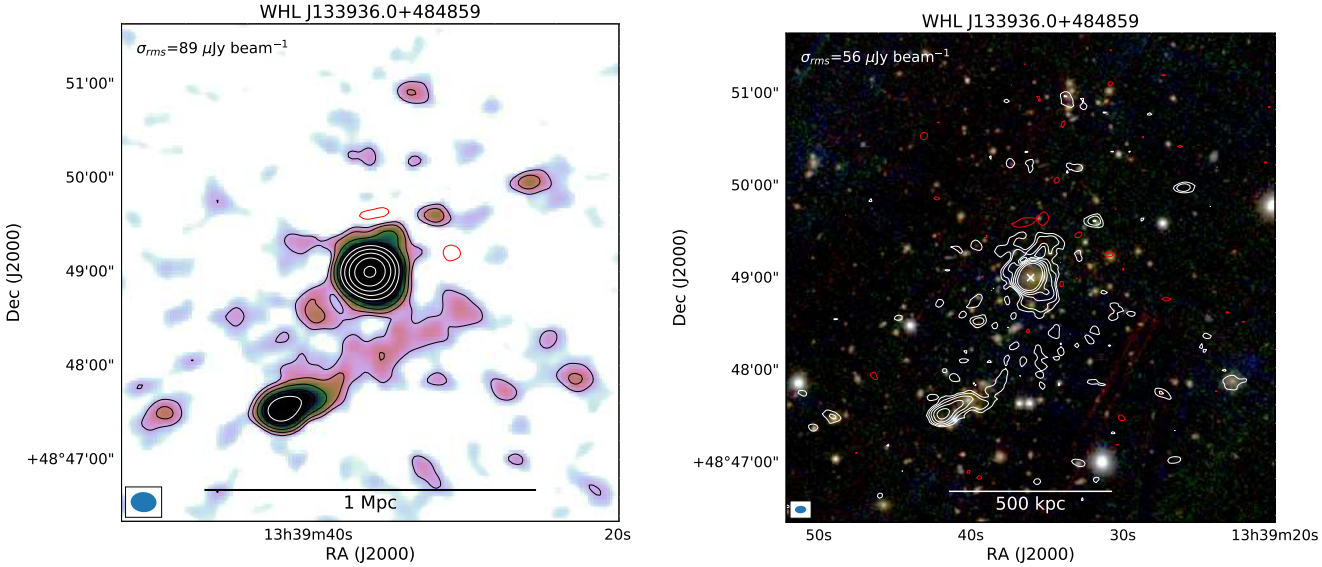

Fig. 23. WHL J133936.0+484859. *Left*: 10″ tapered radio image. *Right*: optical image with robust −0.5 image radio contours. For more details, see the caption of Fig. 5.

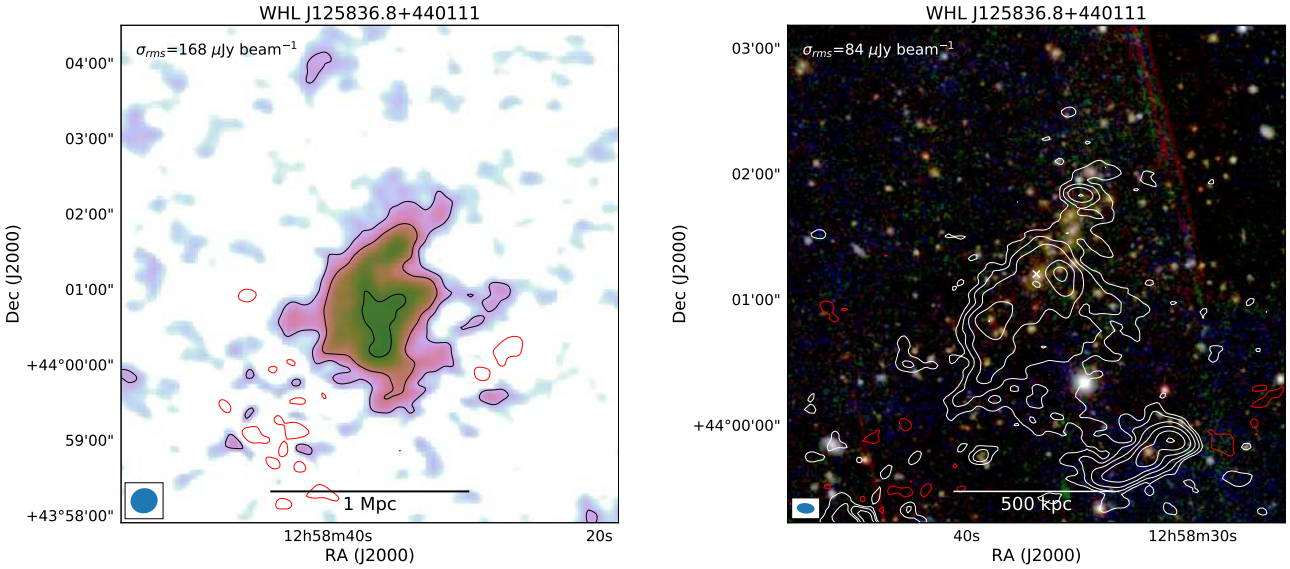

Fig. 24. WHL J125836.8+440111. *Left*: 10″ tapered radio image with compact sources subtracted. *Right*: optical image with robust −0.5 image radio contours. For more details, see the caption of Fig. 5.

Rossetti et al. 2017; Andrade-Santos et al. 2017). The lack of mini-halos in our sample could also be a reflection of the properties of mini-halos at low frequencies. Several low-frequency studies have found the presence of diffuse emission at larger radii, beyond the extent of the mini-halos measured at gigahertz frequencies. Thus, low-frequency studies would be less likely to report mini-halos if size were used as a criterion. Whether this extended emission beyond the "classical" mini-halo extent can be considered as a part of the mini-halo, or is an unrelated component more similar to that of a giant radio halo, is unclear (Bonafede et al. 2014b; Brunetti & Jones 2014; Kale & Parekh 2016; Venturi et al. 2017; Savini et al. 2018, 2019; Kale et al. 2019).

A further complication for the detection of mini-halos is the presence of a radio-bright BCG. The calibration needs to achieve a dynamic range sufficient for a detection. This can be a challenge at low frequencies (see for example Fig. A.5).

The fraction of radio-relic-hosting clusters in PSZ2 is 15 ± 8%. We thus expect 92 ± 46 clusters hosting radio relics in LoTSS. One radio relic is detected in a non-PSZ2 cluster. The expected number of radio relics in the LoTSS survey falls about an order of magnitude below the prediction of Nuza et al. (2012). Predictions are not yet available for more recent models (e.g., Nuza et al. 2017; Brüggen & Vazza 2020).

5.2. $P_{150\,\mathrm{MHz}}$ scaling relations

It is well established that the radio power of giant halos scales with the X-ray luminosity of clusters (e.g., Liang et al. 2000; Cassano et al. 2006, 2013; Kale et al. 2015). A similar scaling exists for the integrated Compton Y parameter, which traces the ICM integrated pressure along the line of sight (Basu 2012; Cassano et al. 2013). Both the X-ray and SZ measurements are proxies of cluster mass. This therefore suggests that the observed

Table 4. Literature sample for $P_{150\,\mathrm{MHz}}$ scaling relations.

Cluster	Alternative name	Redshift	Flux density (mJy)	Frequency (MHz)	Reference
PSZ2 G108.17−11.56	PSZ1 G108.18−11.53	0.336	124 ± 11	147	de Gasperin et al. (2015)
PSZ2 G057.80+88.00	Coma Cluster	0.0231	7200 ± 800	150	Cordey (1985)
PSZ2 G149.22+54.18	Abell 1132	0.1351	178 ± 27	144	Wilber et al. (2018)
PSZ2 G058.29+18.55	RXC J1825.3+3026	0.065	163 ± 47	144	Botteon et al. (2019)
PSZ2 G151.19+48.27	Abell 959	0.2894	94 ± 14	143	Bîrzan et al. (2019)
PSZ2 G071.39+59.54	RXC J1501.3+4220	0.2917	20.2 ± 2.0	144	Wilber et al. (2019)
PSZ2 G139.62+24.18	PSZ1 G139.61+24.20	0.2671	30 ± 4	144	Savini et al. (2018)
PSZ2 G049.22+30.87	RX J1720.1+2638	0.164	165 ± 25	144	Savini et al. (2019)
PSZ2 G138.32-39.82	RXC J0142.0+2131	0.280	32 ± 6	144	Savini et al. (2019)
PSZ2 G226.18+76.79	Abell 1413	0.143	40 ± 7	144	Savini et al. (2019)
PSZ2 G055.59+31.85	Abell 2261	0.224	165 ± 25 [(a)]	144	Savini et al. (2019)
PSZ2 G180.25+21.03	MACS J0717.5+3745	0.546	370 ± 60	147	Bonafede et al. (2018)
PSZ2 G195.75−24.32	Abell 520	0.201	229.7 ± 34.8	145	Hoang et al. (2019a)
PSZ2 G100.14+41.67	Abell 2146	0.232	19.8 ± 5.0 [(b)]	144	Hoang et al. (2019b)
PSZ2 G186.37+37.26	Abell 697	0.282	135 ± 27	153	Macario et al. (2013)
PSZ2 G208.80−30.67	Abell 521	0.247	328 ± 66	153	Macario et al. (2013)
PSZ2 G008.94−81.22	Abell 2744	0.308	415 ± 42	150	George et al. (2017)
PSZ2 G175.69−85.98	Abell 141	0.230	110 ± 11	168	Duchesne et al. (2021)

Notes. [(a)]No flux density uncertainty provided; we adopted an uncertainty of 15%. [(b)]A range of flux densities was provided for the radio halo by Hoang et al. (2019b). We adopted the average value of that range, with the uncertainty reflecting the provided range.

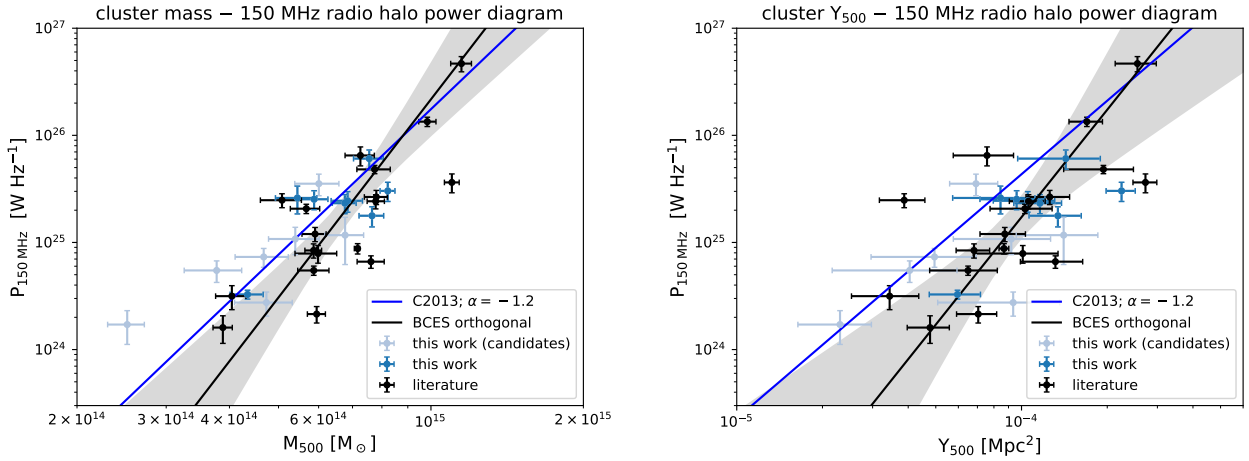

Fig. 25. Radio halo powers plotted against cluster mass proxies. *Left*: distribution of clusters in the mass (M_{500}) 150 MHz radio power ($P_{150\,\mathrm{MHz}}$) plane. The solid black line displays the BCES orthogonal fit (candidate halos were excluded). The shaded region shows the 3σ (99.7% confidence) region of the fit. The blue line is the BCES orthogonal fit from Cassano et al. (2013) scaled with a spectral index of −1.2. *Right*: distribution of clusters in the Y_{500} 150 MHz radio power plane. The plotted symbols and lines represent the same data sets as in the left panel.

correlations originate from an underlying relation between cluster mass and radio power. The explanation for this relation is that a fraction of the gravitational energy released during a merger event, which scales with the cluster host mass, is channeled into the reacceleration of CRs via turbulence (e.g., Cassano & Brunetti 2005; Cassano et al. 2004).

Traditionally, the radio power is computed at a rest-frame frequency of 1.4 GHz ($P_{1.4\,\mathrm{GHz}}$), and all correlation studies have so far used this quantity. With the new LOFAR radio halo detections, it becomes feasible to study this relation at a rest-frame frequency of 150 MHz, with $P_{150\,\mathrm{MHz}}$ given by

$$P_{150\,\mathrm{MHz}} = \frac{4\pi D_{\mathrm{L}}^2 S_{150\,\mathrm{MHz}}}{(1+z)^{\alpha+1}}, \quad (4)$$

where D_{L} is the luminosity distance of the cluster. Because our integrated flux density measurements are obtained at 144 MHz, $P_{150\,\mathrm{MHz}}$ is only marginally affected by the adopted (unknown) radio spectral index.

In this work, we have determined the M_{500}–$P_{150\,\mathrm{MHz}}$ scaling relation for radio halos using clusters from the PSZ2 catalog, which provides an SZ-based mass estimate. The SZ-based mass-selected samples should be less affected by the cluster's dynamical state compared to X-ray-selected samples, which are biased toward relaxed cool-core clusters (e.g., Eckert et al. 2011; Rossetti et al. 2017; Andrade-Santos et al. 2017). We have complemented our new LOFAR measurements with halo detections in the 120–180 MHz range from the literature when reliable measurements are available (see Table 4). These literature values come mostly from previous LOFAR and GMRT studies. A few of them are taken from Murchison Widefield Array (MWA) studies. We did not include all MWA detections, only those with high-quality measurements as indicated from good spectral fits

Table 5. BCES fitted scaling relations for radio halos.

Method	B	σ_B	A	σ_A
M_{500}–$P_{150\,\mathrm{MHz}}$				
Orthogonal	6.13	1.11	1.22	0.12
Bisector	4.67	0.62	1.11	0.09
$Y\|X$	3.84	0.69	1.05	0.09
M_{500}–$P_{150\,\mathrm{MHz}}$ with candidates				
Orthogonal	5.00	0.87	1.21	0.10
Bisector	4.05	0.55	1.11	0.08
$Y\|X$	3.40	0.53	1.04	0.09
Y_{500}–$P_{150\,\mathrm{MHz}}$				
Orthogonal	3.32	0.65	0.74	0.12
Bisector	2.60	0.53	0.74	0.09
$Y\|X$	2.10	0.67	0.74	0.08
Y_{500}–$P_{150\,\mathrm{MHz}}$ with candidates				
Orthogonal	3.05	0.68	0.78	0.10
Bisector	2.43	0.42	0.76	0.08
$Y\|X$	1.98	0.48	0.74	0.07

with low (<2) reduced χ^2 values (George et al. 2017) and from halos not significantly affected by the uncertainties from compact source subtraction.

Following Cassano et al. (2013), we used the following relation

$$\log_{10}\left(\frac{P_{150\,\mathrm{MHz}}}{10^{24.5}\,\mathrm{W\,Hz^{-1}}}\right) = B\log_{10}\left(\frac{M_{500}}{10^{14.9}\,M_{\odot}}\right) + A \quad (5)$$

between radio power and cluster mass. The best fitting parameters were found using the bivariate correlated errors and intrinsic scatter (BCES) orthogonal regression algorithm (Akritas & Bershady 1996; Nemmen et al. 2012). Past work has by default adopted BCES bisector fits (which give consistently flatter slopes), although, as is mentioned by Hogg et al. (2010), bisector fits are not recommended. For comparison with previous work, we also report the results from the BCES bisector and $Y|X$ fits (where X is the independent variable). Our sample approximately covers the mass range $3{-}10 \times 10^{14}\,M_{\odot}$. The results are shown in Fig. 25 (left panel) and Table 5. As is the case for $P_{1.4\,\mathrm{GHz}}$, there is also a clear correlation between between M_{500} and $P_{150\,\mathrm{MHz}}$, and we find a slope of $B = 6.13 \pm 1.11$ (BCES orthogonal). With the candidate halos included, we find somewhat flatter slopes (see Table 5), but, considering the uncertainties, the differences are not significant.

We determined the Y_{500}–$P_{150\,\mathrm{MHz}}$ radio halo scaling relation using the PSZ2 Compton Y parameter. For that, we converted the $Y_{5R_{500}}$ values from Planck Collaboration XXVII (2016) to Y_{500} using $Y_{500} = 0.56\,Y_{5R_{500}}$ (Arnaud et al. 2010). We also converted the units from arcmin^2 to Mpc^2 to facilitate the comparison with Cassano et al. (2013). We applied the same fitting methods as for the M_{500}–$P_{150\,\mathrm{MHz}}$ correlation, using a relation of the form

$$\log_{10}\left(\frac{P_{150\,\mathrm{MHz}}}{10^{24.5}\,\mathrm{W\,Hz^{-1}}}\right) = B\log_{10}\left(\frac{Y_{500}}{10^{-4}\,\mathrm{Mpc^2}}\right) + A. \quad (6)$$

The results are plotted in Fig. 25 (right panel) and are reported in Table 5. The slope of the best fit BCES orthogonal relation is $B = 3.32{\pm}0.65$. The slopes are slightly flatter when the candidate radio halos are included, but, considering the uncertainties, the differences are not significant (see Table 5).

The slopes of the 150 MHz scaling relations we find are steeper than those obtained at 1.4 GHz by Cassano et al. (2013). For Y_{500}–$P_{150\,\mathrm{MHz}}$, they reported $B = 2.28 \pm 0.35$ at 1.4 GHz, compared to $B = 3.32 \pm 0.65$ in this work. For M_{500}–$P_{150\,\mathrm{MHz}}$, they reported a slope of $B = 4.51 \pm 0.78$, compared to our value of $B = 6.13 \pm 1.11$ in this work. However, considering the uncertainties, the slopes at 150 MHz are still consistent with those reported at 1.4 GHz.

Statistical models employing turbulent reacceleration (Cassano et al. 2013) predict $P_{1.4\,\mathrm{GHz}} \propto M_{500}^4$ or steeper, depending on the ICM magnetic field strength with respect to the equivalent magnetic strength of the cosmic microwave background. It should be noted that these models make a number of simplifying assumptions. The most important simplification is that there is no spatial dependence of the magnetic field and acceleration efficiency (see for example Cassano et al. 2010a regarding these "homogeneous models"). Cassano (2010) predicts that the slope of the L_{X}–$P_{1.4\,\mathrm{GHz}}$ scaling relation should steepen by about 0.4 at 150 MHz due to the ultra-steep spectrum halos associated with intermediate mass galaxy clusters. Using the fact that $L_{\mathrm{X}} \propto M_{500}^2$, we thus expect a steepening of about 0.8 for the M_{500}–$P_{150\,\mathrm{MHz}}$ scaling relation. In addition, the scatter around the scaling relations should increase. Interestingly, the slopes we find at 150 MHz are indeed steeper than at 1.4 GHz, in line with this prediction. That said, the uncertainties on the determined slopes are still too large for any firm claim. For this reason, extending the sample size and mass range will be crucially important for confirming this result.

One of the limitations of our presented analysis is that, due to the small sample size, we did not apply any cut in mass or redshift. For a more detailed comparison with the Cassano et al. (2013) results, a similar redshift and mass cut should be applied. We also note that our sample contains three clusters (Abell 1413, PSZ1 G139.61+24.20, and RX J1720.1+2638) with diffuse sources that were previously classified as mini-halos. Since the diffuse emission in these clusters turns out to be more extended[4] at low frequencies than the typical scale of mini-halos, we have included them in our sample. Further investigations are also required to determine how the low-frequency scaling relations and occurrence rates depend on the cluster dynamical state. Another limitation of our derived scaling relations is the inclusion of literature values that were obtained in a variety of ways, that is, with different methods adopted to measure the integrated flux density. That said, the literature values do not seem to be strongly biased either high or low when compared to the measurements obtained in this work for clusters with similar masses, and hence this should not have a large effect on the derived slopes. This limitation will be removed in future work when larger LOFAR samples become available.

A comparison between the 150 MHz and 1.4 GHz relations allowed us to investigate the average spectral index of radio halos in this frequency range. We find that when using $\alpha = -1.2$ a good match is obtained between the two M_{500}–$P_{150\,\mathrm{MHz}}$ scaling relations. For Y_{500}–$P_{150\,\mathrm{MHz}}$, a slightly flatter spectral index seems to be preferred (the blue line in the right panel of Fig. 25 is located mostly above our best fit). Giovannini et al. (2009) obtained a medium spectral index of -1.3 for radio halos between 325 MHz and 1.4 GHz, in reasonable agreement our results. However, for a better assessment of the radio halo spectral indices, detailed cluster-to-cluster comparisons are required. In particular, the scaling relation from Cassano et al. (2013) that we used did not include USSRHs. This could have a direct effect on the derived spectral indices when comparing to a low-frequency sample that potentially contains a significant number of USSRHs.

[4] This also includes Abell 1413 based on new LoTSS data.

6. Conclusions

We have presented a method to extract and recalibrate targets of interest from the LoTSS survey based on the `DDF-pipeline` software. This method allows joint imaging of data from multiple pointings and an improvement in calibration accuracy. It also enables the fast imaging of targets without covering the full FoV of a LOFAR observation.

We applied the above scheme to a total of 41 clusters – 26 *Planck* PSZ2 clusters and 15 other clusters – located in the HETDEX Spring region. In total we detect ten radio halos. Five clusters host radio relics. We also report 12 candidate radio halos. The occurrence fraction of radio halos in PSZ2 clusters is $31 \pm 11\%$, or $62 \pm 15\%$ if we include the candidate radio halos. The fraction of PSZ2 clusters with some form of diffuse radio emission is $73 \pm 17\%$. The relatively large number of candidate radio halos results from the difficulties in unambiguously classifying the emission. Based on the above numbers, we expect to find at least 183 ± 65 radio halos from the analysis of PSZ2 clusters in the LoTSS survey. Considering all clusters and candidate radio halos, we expect 400–500 halos to be found in the completed LoTSS survey.

We determined, for the first time, the radio halo scaling relations between the cluster mass (Y_{SZ}) and the 150 MHz radio power ($P_{150\,MHz}$). The slopes for these scaling relations are slightly steeper than those determined at 1.4 GHz. This is in line with predictions, however, considering the uncertainties, this is not a statistically significant result. In a future work that uses a larger sample, we will present a more detailed statistical analysis of the properties of the diffuse radio sources in the LoTSS survey.

Acknowledgements. We would like to thank the anonymous referee for useful comments. This paper is based on data obtained with the International LOFAR Telescope (ILT) under project codes LC2_038 and LC3_008. LOFAR (van Haarlem et al. 2013) is the LOw Frequency ARray designed and constructed by ASTRON. It has observing, data processing, and data storage facilities in several countries, which are owned by various parties (each with their own funding sources) and are collectively operated by the ILT foundation under a joint scientific policy. The ILT resources have benefited from the following recent major funding sources: CNRS-INSU, Observatoire de Paris and Université d'Orléans, France; BMBF, MIWF-NRW, MPG, Germany; Science Foundation Ireland (SFI), Department of Business, Enterprise and Innovation (DBEI), Ireland; NWO, The Netherlands; The Science and Technology Facilities Council, UK; Ministry of Science and Higher Education, Poland; The Istituto Nazionale di Astrofisica (INAF), Italy. This research made use of the Dutch national e-infrastructure with support of the SURF Cooperative (e-infra 180169) and the LOFAR e-infra group. The Jülich LOFAR Long Term Archive and the GermanLOFAR network are both coordinated and operated by the Jülich Supercomputing Centre (JSC), and computing resources on the supercomputer JUWELS at JSC were provided by the Gauss Centre for Supercomputinge.V. (grant CHTB00) through the John von Neumann Institute for Computing (NIC). This research made use of the University of Hertfordshire high-performance computing facility (`http://uhhpc.herts.ac.uk`) and the LOFAR-UK computing facility located at the University of Hertfordshire and supported by STFC [ST/P000096/1], and of the Italian LOFAR IT computing infrastructure supported and operated by INAF, and by the Physics Department of Turin University (under an agreement with Consorzio Interuniversitario per la Fisica Spaziale) at the C3S Supercomputing Centre, Italy. This research made use of Astropy (`http://www.astropy.org`), a community-developed core Python package for Astronomy (Astropy Collaboration 2013, 2018). RJvW and ABott acknowledge support from the VIDI research programme with project number 639.042.729, which is financed by the Netherlands Organisation for Scientific Research (NWO). GB, RC, and FG acknowledge support from INAF mainstream project "Galaxy Clusters Science with LOFAR" 1.05.01.86.05. ABon and EB ackowledge support from the ERC-Stg DRANOEL n. 714245 and from the Italian MIUR grant FARE "SMS". The Pan-STARRS1 Surveys (PS1) and the PS1 public science archive have been made possible through contributions by the Institute for Astronomy, the University of Hawaii, the Pan-STARRS Project Office, the Max-Planck Society and its participating institutes, the Max Planck Institute for Astronomy, Heidelberg and the Max Planck Institute for Extraterrestrial Physics, Garching, The Johns Hopkins University, Durham University, the University of Edinburgh, the Queen's University Belfast, the Harvard-Smithsonian Center for Astrophysics, the Las Cumbres Observatory Global Telescope Network Incorporated, the National Central University of Taiwan, the Space Telescope Science Institute, the National Aeronautics and Space Administration under Grant No. NNX08AR22G issued through the Planetary Science Division of the NASA Science Mission Directorate, the National Science Foundation Grant No. AST-1238877, the University of Maryland, Eotvos Lorand University (ELTE), the Los Alamos National Laboratory, and the Gordon and Betty Moore Foundation. This research has made use of data obtained from the *Chandra* Data Archive and the *Chandra* Source Catalog, and software provided by the *Chandra* X-ray Center (CXC) in the application packages CIAO, ChIPS, and Sherpa. Based on observations obtained with *XMM-Newton*, an ESA science mission with instruments and contributions directly funded by ESA Member States and NASA.

References

Abell, G. O. 1958, ApJS, 3, 211
Ackermann, M., Ajello, M., Albert, A., et al. 2016, ApJ, 819, 149
Akamatsu, H., & Kawahara, H. 2013, PASJ, 65, 16
Akritas, M. G., & Bershady, M. A. 1996, ApJ, 470, 706
Andrade-Santos, F., Jones, C., Forman, W. R., et al. 2017, ApJ, 843, 76
Arnaud, M., Pratt, G. W., Piffaretti, R., et al. 2010, A&A, 517, A92
Astropy Collaboration (Robitaille, T. P., et al.) 2013, A&A, 558, A33
Astropy Collaboration (Price-Whelan, A. M., et al.) 2018, AJ, 156, 123
Bagchi, J., Durret, F., Neto, G. B. L., & Paul, S. 2006, Science, 314, 791
Basu, K. 2012, MNRAS, 421, L112
Bîrzan, L., Rafferty, D. A., Cassano, R., et al. 2019, MNRAS, 487, 4775
Blandford, R., & Eichler, D. 1987, Phys. Rep., 154, 1
Blasi, P., & Colafrancesco, S. 1999, Astropart. Phys., 12, 169
Bonafede, A., Intema, H. T., Brüggen, M., et al. 2014a, ApJ, 785, 1
Bonafede, A., Intema, H. T., Bruggen, M., et al. 2014b, MNRAS, 444, L44
Bonafede, A., Cassano, R., Brüggen, M., et al. 2017, MNRAS, 470, 3465
Bonafede, A., Brüggen, M., Rafferty, D., et al. 2018, MNRAS, 478, 2927
Bonnassieux, E., Tasse, C., Smirnov, O., & Zarka, P. 2018, A&A, 615, A66
Boschin, W., Girardi, M., & Gastaldello, F. 2020, MNRAS, 492, 2405
Botteon, A., Gastaldello, F., Brunetti, G., & Dallacasa, D. 2016a, MNRAS, 460, L84
Botteon, A., Gastaldello, F., Brunetti, G., & Kale, R. 2016b, MNRAS, 463, 1534
Botteon, A., Shimwell, T. W., Bonafede, A., et al. 2018, MNRAS, 478, 885
Botteon, A., Cassano, R., Eckert, D., et al. 2019, A&A, 630, A77
Botteon, A., Brunetti, G., Ryu, D., & Roh, S. 2020a, A&A, 634, A64
Botteon, A., Brunetti, G., van Weeren, R. J., et al. 2020b, ApJ, 897, 93
Botteon, A., van Weeren, R. J., Brunetti, G., et al. 2020c, MNRAS, 499, L11
Boxelaar, J. M., van Weeren, R. J., & Botteon, A. 2021, Astron. Comput., 35, 100464
Briggs, D. S. 1995, Am. Astron. Soc. Meet. Abstr., 187, 112.02
Brüggen, M., & Vazza, F. 2020, MNRAS, 493, 2306
Brüggen, M., Rafferty, D., Bonafede, A., et al. 2018, MNRAS, 477, 3461
Brunetti, G., & Jones, T. W. 2014, Int. J. Mod. Phys. D, 23, 30007
Brunetti, G., & Lazarian, A. 2007, MNRAS, 378, 245
Brunetti, G., & Lazarian, A. 2011, MNRAS, 410, 127
Brunetti, G., & Vazza, F. 2020, Phys. Rev. Lett., 124, 051101
Brunetti, G., Setti, G., Feretti, L., & Giovannini, G. 2001, MNRAS, 320, 365
Brunetti, G., Venturi, T., Dallacasa, D., et al. 2007, ApJ, 670, L5
Brunetti, G., Giacintucci, S., Cassano, R., et al. 2008, Nature, 455, 944
Brunetti, G., Blasi, P., Reimer, O., et al. 2012, MNRAS, 426, 956
Brunetti, G., Rudnick, L., Cassano, R., et al. 2013, A&A, 558, A52
Brunetti, G., Zimmer, S., & Zandanel, F. 2017, MNRAS, 472, 1506
Cassano, R. 2010, A&A, 517, A10
Cassano, R., & Brunetti, G. 2005, MNRAS, 357, 1313
Cassano, R., Brunetti, G., & Setti, G. 2004, J. Korean Astron. Soc., 37, 589
Cassano, R., Brunetti, G., & Setti, G. 2006, MNRAS, 369, 1577
Cassano, R., Brunetti, G., Röttgering, H. J. A., & Brüggen, M. 2010a, A&A, 509, A68
Cassano, R., Ettori, S., Giacintucci, S., et al. 2010b, ApJ, 721, L82
Cassano, R., Brunetti, G., Norris, R. P., et al. 2012, A&A, 548, A100
Cassano, R., Ettori, S., Brunetti, G., et al. 2013, ApJ, 777, 141
Cassano, R., Botteon, A., Di Gennaro, G., et al. 2019, ApJ, 881, L18
Chambers, K. C., Magnier, E. A., Metcalfe, N., et al. 2016, ArXiv e-prints [arXiv:1612.05560]
Clarke, A. O., Scaife, A. M. M., Shimwell, T., et al. 2019, A&A, 627, A176
Cordey, R. A. 1985, MNRAS, 215, 437
Corwin, H. G., Jr 1974, AJ, 79, 1356
Cuciti, V., Cassano, R., Brunetti, G., et al. 2015, A&A, 580, A97
David, L. P., & Kempner, J. 2004, ApJ, 613, 831

de Gasperin, F., Intema, H. T., van Weeren, R. J., et al. 2015, MNRAS, 453, 3483
de Gasperin, F., Intema, H. T., Shimwell, T. W., et al. 2017, Sci. Adv., 3
de Gasperin, F., Dijkema, T. J., Drabent, A., et al. 2019, A&A, 622, A5
Dennison, B. 1980, ApJ, 239, L93
Di Gennaro, G., van Weeren, R. J., Hoeft, M., et al. 2018, ApJ, 865, 24
Di Gennaro, G., van Weeren, R. J., Andrade-Santos, F., et al. 2019, ApJ, 873, 64
Di Gennaro, G., van Weeren, R. J., Brunetti, G., et al. 2021, Nat. Astron., 5, 268
Dolag, K., & Enßlin, T. A. 2000, A&A, 362, 151
Duchesne, S. W., Johnston-Hollitt, M., Offringa, A. R., et al. 2021, PASA, 38, e010
Eckert, D., Molendi, S., & Paltani, S. 2011, A&A, 526, A79
Enßlin, T. A., & Brüggen, M. 2002, MNRAS, 331, 1011
Enßlin, T. A., & Gopal-Krishna 2001, A&A, 366, 26
Enßlin, T. A., Biermann, P. L., Klein, U., & Kohle, S. 1998, A&A, 332, 395
Feretti, L., Giovannini, G., Govoni, F., & Murgia, M. 2012, A&ARv, 20, 54
Finoguenov, A., Sarazin, C. L., Nakazawa, K., Wik, D. R., & Clarke, T. E. 2010, ApJ, 715, 1143
Fujita, Y., & Ohira, Y. 2013, MNRAS, 428, 599
Fujita, Y., Kohri, K., Yamazaki, R., & Kino, M. 2007, ApJ, 663, L61
Gal, R. R., de Carvalho, R. R., Lopes, P. A. A., et al. 2003, AJ, 125, 2064
George, L. T., Dwarakanath, K. S., Johnston-Hollitt, M., et al. 2017, MNRAS, 467, 936
Giacintucci, S., Venturi, T., Macario, G., et al. 2008, A&A, 486, 347
Giacintucci, S., Markevitch, M., Venturi, T., et al. 2014, ApJ, 781, 9
Giacintucci, S., Markevitch, M., Cassano, R., et al. 2017, ApJ, 841, 71
Giovannini, G., Bonafede, A., Feretti, L., et al. 2009, A&A, 507, 1257
Gitti, M., Brunetti, G., Feretti, L., & Setti, G. 2004, A&A, 417, 1
Govoni, F., Ferrari, C., Feretti, L., et al. 2012, A&A, 545, A74
Govoni, F., Orrù, E., Bonafede, A., et al. 2019, Science, 364, 981
Gu, L., Akamatsu, H., Shimwell, T. W., et al. 2019, Nat. Astron., 3, 838
Hao, J., McKay, T. A., Koester, B. P., et al. 2010, ApJS, 191, 254
Hardcastle, M. J., Croston, J. H., Shimwell, T. W., et al. 2019, MNRAS, 488, 3416
Hoang, D. N., Shimwell, T. W., van Weeren, R. J., et al. 2019a, A&A, 622, A20
Hoang, D. N., Shimwell, T. W., van Weeren, R. J., et al. 2019b, A&A, 622, A21
Hoeft, M., Dumba, C., Drabent, A., et al. 2020, A&A, submitted [arXiv:2010.10331]
Hogg, D. W., Bovy, J., & Lang, D. 2010, ArXiv e-prints [arXiv:1008.4686]
Itahana, M., Takizawa, M., Akamatsu, H., et al. 2017, PASJ, 69, 88
Jones, F. C., & Ellison, D. C. 1991, Space Sci. Rev., 58, 259
Joye, W. A., & Mandel, E. 2003, in Astronomical Data Analysis Software and Systems XII, eds. H. E. Payne, R. I. Jedrzejewski, & R. N. Hook, ASP Conf. Ser., 295, 489
Kale, R., & Parekh, V. 2016, MNRAS, 459, 2940
Kale, R., Venturi, T., Giacintucci, S., et al. 2013, A&A, 557, A99
Kale, R., Venturi, T., Giacintucci, S., et al. 2015, A&A, 579, A92
Kale, R., Shende, K. M., & Parekh, V. 2019, MNRAS, 486, L80
Kang, H., & Ryu, D. 2011, ApJ, 734, 18
Kang, H., Ryu, D., & Jones, T. W. 2012, ApJ, 756, 97
Kempner, J. C., & Sarazin, C. L. 2001, ApJ, 548, 639
Keshet, U., & Loeb, A. 2010, ApJ, 722, 737
Koester, B. P., McKay, T. A., Annis, J., et al. 2007, ApJ, 660, 239
Liang, H., Hunstead, R. W., Birkinshaw, M., & Andreani, P. 2000, ApJ, 544, 686
Locatelli, N. T., Rajpurohit, K., Vazza, F., et al. 2020, MNRAS, 496, L48
Macario, G., Venturi, T., Intema, H. T., et al. 2013, A&A, 551, A141
Malkov, M. A., & O'C Drury, L., 2001, Rep. Progr. Phys., 64, 429
Mandal, S., Intema, H. T., van Weeren, R. J., et al. 2020, A&A, 634, A4
Mann, A. W., & Ebeling, H. 2012, MNRAS, 420, 2120
Markevitch, M., Govoni, F., Brunetti, G., & Jerius, D. 2005, ApJ, 627, 733
Mazzotta, P., & Giacintucci, S. 2008, ApJ, 675, L9
Miniati, F. 2015, ApJ, 800, 60
Morandi, A., Sun, M., Forman, W., & Jones, C. 2015, MNRAS, 450, 2261
Murgia, M., Govoni, F., Markevitch, M., et al. 2009, A&A, 499, 679
Nemmen, R. S., Georganopoulos, M., Guiriec, S., et al. 2012, Science, 338, 1445
Nuza, S. E., Hoeft, M., van Weeren, R. J., Gottlöber, S., & Yepes, G. 2012, MNRAS, 420, 2006
Nuza, S. E., Gelszinnis, J., Hoeft, M., & Yepes, G. 2017, MNRAS, 470, 240
Offringa, A. R. 2010, Astrophysics Source Code Library [record ascl:1010.017]
Offringa, A. R. 2016, A&A, 595, A99
Offringa, A. R., & Smirnov, O. 2017, MNRAS, 471, 301
Offringa, A. R., de Bruyn, A. G., Biehl, M., et al. 2010, MNRAS, 405, 155
Offringa, A. R., van de Gronde, J. J., & Roerdink, J. B. T. M. 2012, A&A, 539, A95
Offringa, A. R., McKinley, B., Hurley-Walker, N., et al. 2014, MNRAS, 444, 606
Ogrean, G. A., & Brüggen, M. 2013, MNRAS, 433, 1701
Paul, S., Salunkhe, S., Sonkamble, S., et al. 2020, A&A, 633, A59
Petrosian, V. 2001, ApJ, 557, 560
Pfrommer, C., & Enßlin, T. A. 2004, A&A, 413, 17
Piffaretti, R., Arnaud, M., Pratt, G. W., Pointecouteau, E., & Melin, J.-B. 2011, A&A, 534, A109
Pinzke, A., Oh, S. P., & Pfrommer, C. 2013, MNRAS, 435, 1061
Pinzke, A., Oh, S. P., & Pfrommer, C. 2017, MNRAS, 465, 4800
Planck Collaboration XXVII 2016, A&A, 594, A27
Rajpurohit, K., Hoeft, M., van Weeren, R. J., et al. 2018, ApJ, 852, 65
Rajpurohit, K., Hoeft, M., Vazza, F., et al. 2020, A&A, 636, A30
Richard, J., Pei, L., Limousin, M., Jullo, E., & Kneib, J. P. 2009, A&A, 498, 37
Rizza, E., Burns, J. O., Ledlow, M. J., et al. 1998, MNRAS, 301, 328
Rossetti, M., Gastaldello, F., Eckert, D., et al. 2017, MNRAS, 468, 1917
Rudnick, L., & Lemmerman, J. A. 2009, ApJ, 697, 1341
Savini, F., Bonafede, A., Brüggen, M., et al. 2018, MNRAS, 478, 2234
Savini, F., Bonafede, A., Brüggen, M., et al. 2019, A&A, 622, A24
Sebastian, B., Lal, D. V., & Pramesh Rao, A. 2017, AJ, 154, 169
Sereno, M., Giocoli, C., Izzo, L., et al. 2018, Nat. Astron., 2, 744
Shimwell, T. W., Markevitch, M., Brown, S., et al. 2015, MNRAS, 449, 1486
Shimwell, T. W., Röttgering, H. J. A., Best, P. N., et al. 2017, A&A, 598, A104
Shimwell, T. W., Tasse, C., Hardcastle, M. J., et al. 2019, A&A, 622, A1
Slee, O. B., Roy, A. L., Murgia, M., Andernach, H., & Ehle, M. 2001, AJ, 122, 1172
Srivastava, S., & Singal, A. K. 2020, MNRAS, 493, 3811
Tasse, C. 2014a, ArXiv e-prints [arXiv:1410.8706]
Tasse, C. 2014b, A&A, 566, A127
Tasse, C., Hugo, B., Mirmont, M., et al. 2018, A&A, 611, A87
Tasse, C., Shimwell, T., Hardcastle, M. J., et al. 2021, A&A, 648, A1
Tikhonov, N. A., & Karachentsev, I. D. 1998, A&AS, 128, 325
Umetsu, K., Broadhurst, T., Zitrin, A., Medezinski, E., & Hsu, L.-Y. 2011, ApJ, 729, 127
van der Tol, S., Veenboer, B., & Offringa, A. R. 2018, A&A, 616, A27
van Diepen, G., & Dijkema, T. J. 2018, Astrophysics Source Code Library [record ascl:1804.003]
van Haarlem, M. P., Wise, M. W., Gunst, A. W., et al. 2013, A&A, 556, A2
van Weeren, R. J., Brüggen, M., Röttgering, H. J. A., et al. 2011, A&A, 533, A35
van Weeren, R. J., Röttgering, H. J. A., Intema, H. T., et al. 2012, A&A, 546, A124
van Weeren, R. J., Brunetti, G., Brüggen, M., et al. 2016a, ApJ, 818, 204
van Weeren, R. J., Williams, W. L., Hardcastle, M. J., et al. 2016b, ApJS, 223, 2
van Weeren, R. J., Andrade-Santos, F., Dawson, W. A., et al. 2017, Nat. Astron., 1, 0005
van Weeren, R. J., de Gasperin, F., Akamatsu, H., et al. 2019, Space Sci. Rev., 215, 16
Vazza, F., & Brüggen, M. 2014, MNRAS, 437, 2291
Vazza, F., Brüggen, M., Wittor, D., et al. 2016, MNRAS, 459, 70
Venturi, T., Giacintucci, S., Dallacasa, D., et al. 2008, A&A, 484, 327
Venturi, T., Giacintucci, S., & Dallacasa, D. 2011, J. Astrophys. Astron., 32, 501
Venturi, T., Giacintucci, S., Dallacasa, D., et al. 2013, A&A, 551, A24
Venturi, T., Rossetti, M., Brunetti, G., et al. 2017, A&A, 603, A125
Wen, Z. L., Han, J. L., & Liu, F. S. 2012, ApJS, 199, 34
Wilber, A., Brüggen, M., Bonafede, A., et al. 2018, MNRAS, 473, 3536
Wilber, A., Brüggen, M., Bonafede, A., et al. 2019, A&A, 622, A25
Yuan, Z. S., & Han, J. L. 2020, MNRAS, 497, 5485
ZuHone, J. A., Markevitch, M., Brunetti, G., & Giacintucci, S. 2013, ApJ, 762, 78
Zwicky, F., Herzog, E., Wild, P., Karpowicz, M., & Kowal, C. T. 1961, Catalogue of galaxies and of clusters of galaxies, (Pasadena: California Institute of Technology), I

Appendix A: Additional clusters

In this appendix we present radio images of clusters without diffuse emission. In addition, clusters with previously known diffuse emission are described.

A.1. PSZ2 G084.10+58.72

The *XMM-Newton* image of this distant cluster ($z = 0.73$) shows a disturbed system with a 1 Mpc bar-like structure north of the cluster center (see Fig. A.1). A hint of centrally located diffuse emission is seen in the image with compact sources subtracted. This emission extends on scales of about 0.5 Mpc. We therefore classify it as a candidate radio halo with $S_{144} = 4.2 \pm 1.2$ mJy. Di Gennaro et al. (2021) also reported a hint of diffuse emission in this cluster.

A.2. PSZ2 G086.93+53.18

Our low-resolution LOFAR image reveals diffuse emission with a largest extent of about 0.6 Mpc in this $z = 0.6752$ cluster (see Fig. A.2). This emission is centrally located, and we therefore classify it as a radio halo with a flux density of 12.2 ± 3.6 mJy. This is consistent, within the uncertainties, with the value reported by Di Gennaro et al. (2021), who presented the discovery of a radio halo in this cluster. Yuan & Han (2020) classify the cluster as a disturbed system based on *Chandra* observations.

A.3. PSZ2 G087.39+50.92

The LOFAR image shows a compact AGN associated with the central BCG of this distant cluster (Fig. A.3). No diffuse radio emission is detected. We note that one of the LoTSS observations had to be discarded due to bad ionospheric conditions.

A.4. PSZ2 G088.98+55.07

A compact radio source is detected at the center of this distant cluster ($z = 0.7023$). An optical image with radio contours overlaid is shown in Fig. A.4. We do not find evidence for diffuse emission in this cluster. However, we note that the LOFAR observations were affected by bad ionospheric conditions.

A.5. PSZ2 G096.14+56.24, Abell 1940

No diffuse radio emission is detected Abell 1940. The image dynamic range is limited by the bright double-lobed radio source associated with the BCG. An optical image with radio contours overlaid is shown in Fig. A.5.

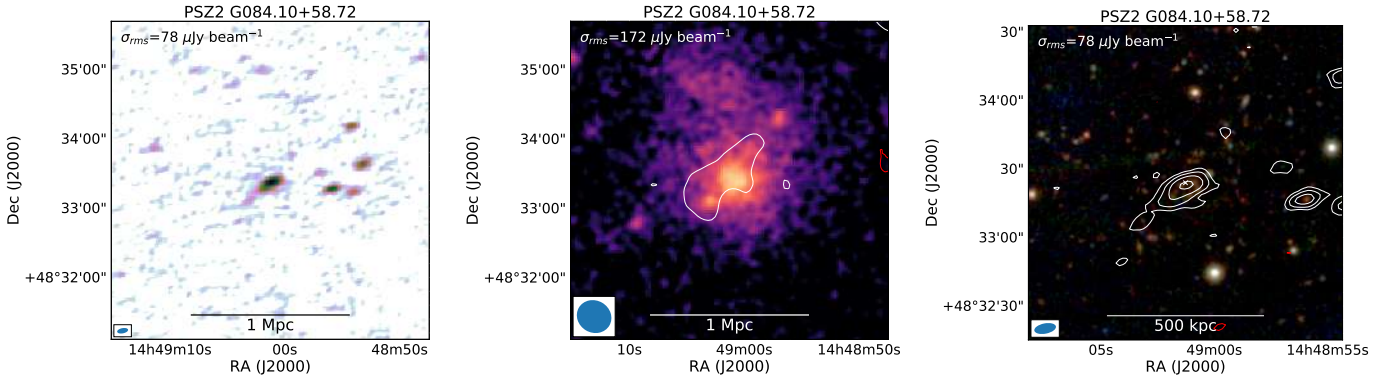

Fig. A.1. PSZ2 G084.10+58.72. *Left*: robust −0.5 radio image. *Middle*: *XMM-Newton* X-ray image with 15″ tapered radio contours (compact sources were subtracted). *Right*: optical image with robust −0.5 image radio contours. For more details, see the caption of Fig. 5.

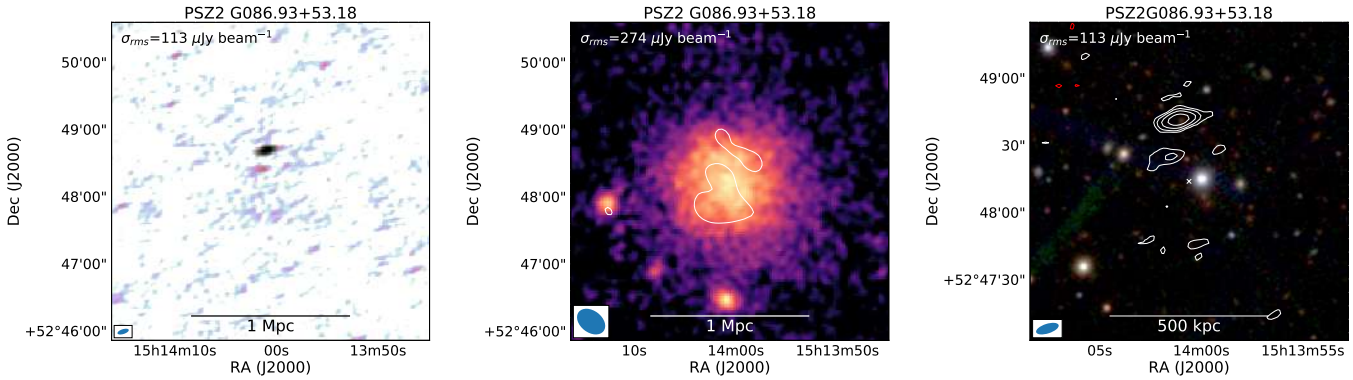

Fig. A.2. PSZ2 G086.93+53.18. *Left*: robust −0.5 radio image. *Middle*: *XMM-Newton* X-ray image with 15″ tapered radio contours (compact sources were subtracted). *Right*: optical image with robust −0.5 image radio contours. For more details, see the caption of Fig. 5.

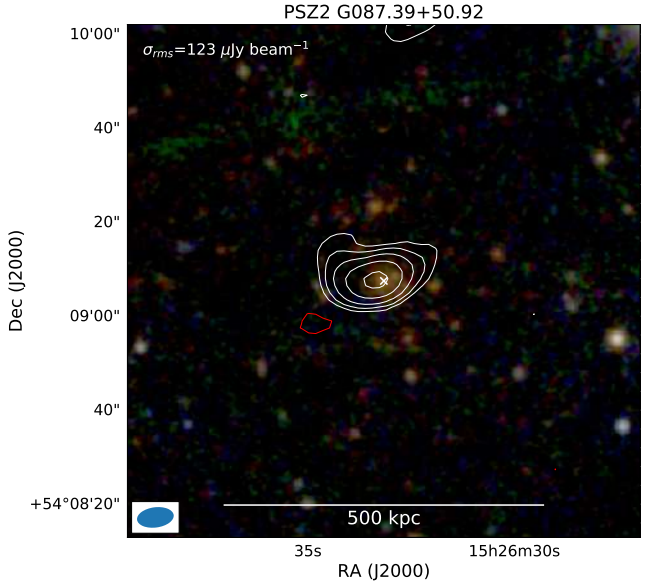

Fig. A.3. PSZ2 G087.39+50.92. Optical image with robust −0.5 image radio contours. For more details, see the caption of Fig. 5.

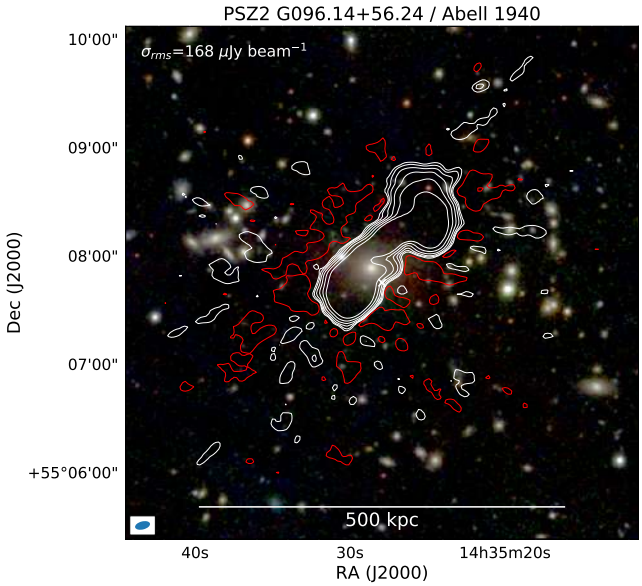

Fig. A.5. PSZ2 G096.14+56.24, Abell 1940. Optical image with robust −0.5 image radio contours. For more details, see the caption of Fig. 5.

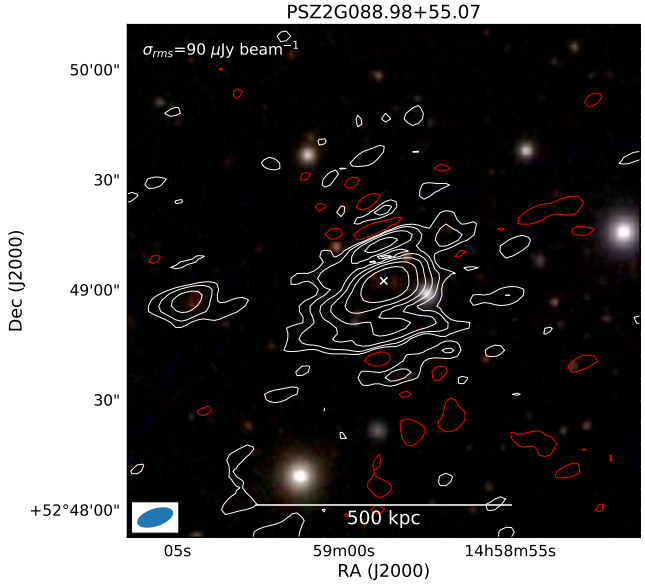

Fig. A.4. PSZ2 G088.98+55.07. Optical image with robust −0.5 image radio contours. For more details, see the caption of Fig. 5.

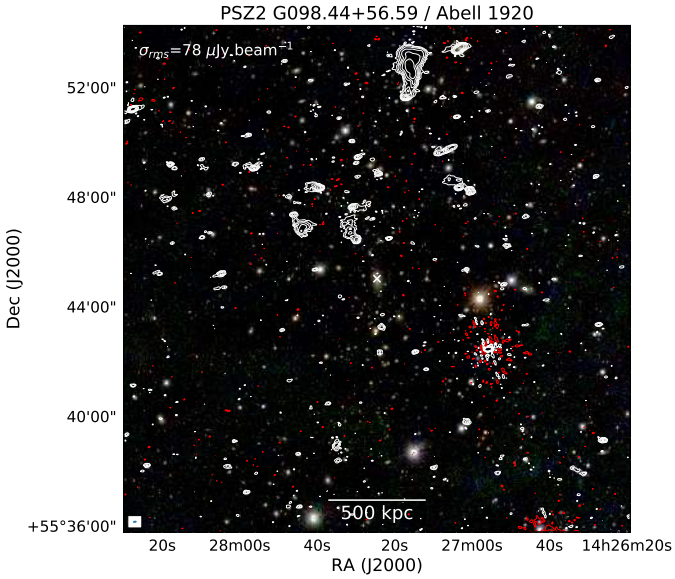

Fig. A.6. PSZ2 G098.44+56.59, Abell 1920. Optical image with robust −0.5 image radio contours. For more details, see the caption of Fig. 5.

A.6. PSZ2 G098.44+56.59, Abell 1920

Several tailed radio galaxies are visible in the cluster region, but no diffuse emission is detected (see Fig. A.6).

A.7. PSZ2 G099.86+58.45

PSZ2 G099.86+58.45 is a massive cluster ($M_{500} = 6.85^{+0.48}_{-0.49} \times 10^{14}\,M_{\odot}$) with a global temperature of $8.9^{+2.8}_{-1.1}$ keV (Sereno et al. 2018). The cluster is known to be undergoing a merger event. The discovery of a 1 Mpc radio halo in this distant cluster ($z = 0.616$; see Fig. A.7) was reported by Cassano et al. (2019) based on LOFAR data. From an elliptical fit, we determine $S_{144} = 14.7 \pm 3.2$ mJy. This number is somewhat lower than the 25.3 ± 5.7 reported by Cassano et al. (2019). This difference is caused by a small extension of the radio halo around compact source B (discussed by Cassano et al. 2019). If this region is included, the two measurements are consistent with each other, given the uncertainties.

A.8. PSZ2 G107.10+65.32, Abell 1758

Abell 1758 is composed of two main clusters, Abell 1758N and Abell 1758S (see Fig. A.8). These two clusters appear to be in a pre-merger phase (Rizza et al. 1998; David & Kempner 2004). The individual clusters themselves are disturbed and already undergoing their own merger events. The presence of a radio halo in A1758N was first reported by Kempner & Sarazin (2001) and further studied by Giovannini et al. (2009) and Venturi et al. (2013).

Botteon et al. (2018) studied this cluster with LOFAR HBA observations, a subset of the data used here. They measured

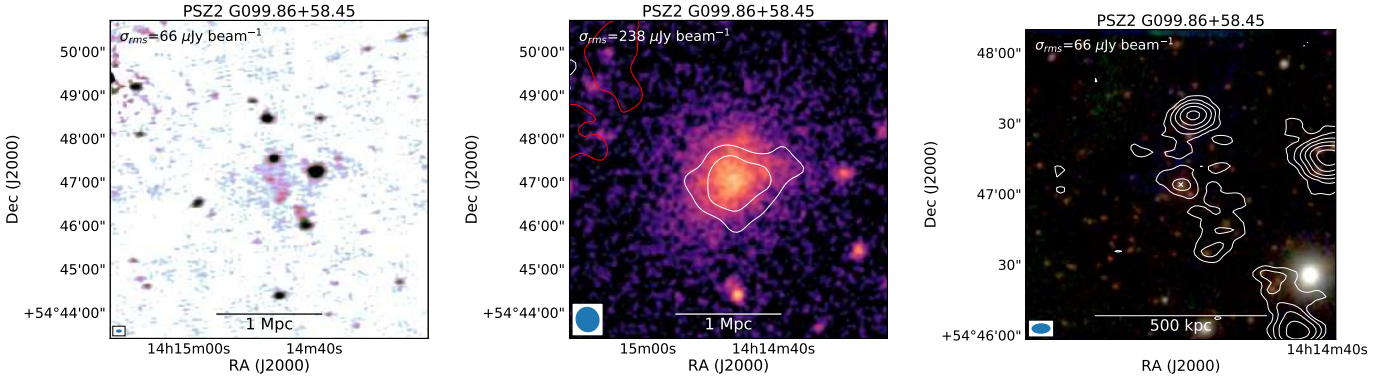

Fig. A.7. PSZ2 G099.86+58.45. *Left*: robust −0.5 radio image. *Middle*: *XMM-Newton* X-ray image with 30″ tapered radio contours (compact sources were subtracted). *Right*: optical image with robust −0.5 image radio contours. For more details, see the caption of Fig. 5.

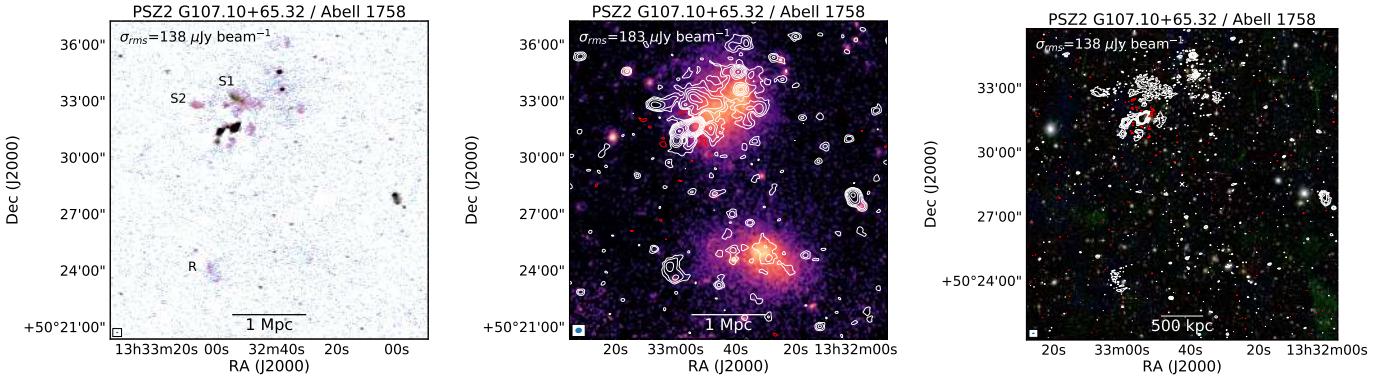

Fig. A.8. PSZ2 G107.10+65.32, Abell 1758. *Left*: robust −0.5 radio image. *Middle*: *Chandra* X-ray image with 10″ tapered radio contours. *Right*: optical image with robust −0.5 image radio contours. For more details, see the caption of Fig. 5.

a size of about 2 Mpc for the A1758N radio halo and discovered a 1.6 Mpc radio halo and a ∼0.5 Mpc relic (labeled R) in A1758S. In addition, a hint of faint emission was detected between A1758N and A1758S. This "radio bridge" was subsequently confirmed by Botteon et al. (2020c). Two bright patches, labeled S1 and S2, were found in A1758N. They are not directly associated with an optical counterpart and possibly trace compressed AGN fossil plasma.

For the radio halo in A1758N, we find a flux of 123 ± 25 mJy based on the elliptical model fit. This value is lower than the 307 ± 63 mJy measured earlier by Botteon et al. (2020c). The reason for this difference is that we excluded the region around sources A and B (see Botteon et al. 2018) and S1 and S2. This particular case highlights the difficulties in classifying and separating the emission from different components with uncertain identifications. For the southern radio halo we determine S_{144} = 63 ± 14 mJy from the elliptical model, consistent with the value reported by Botteon et al. (2018). For a more comprehensive description of the LOFAR findings, we refer the reader to Botteon et al. (2018, 2020c).

A.9. PSZ2 G114.99+70.36, Abell 1682

The presence of diffuse emission in this cluster was first reported by Venturi et al. (2008) and subsequently studied in more detail by Venturi et al. (2011, 2013) and Macario et al. (2013). LOFAR observations show complex diffuse emission extending over a region of more than 1 Mpc (see Fig. A.9). The *Chandra* X-ray image displays a disturbed ICM, indicating that the cluster is undergoing a merger event. The LOFAR results were presented in Clarke et al. (2019). Some of the structures in the cluster are related to distorted and tailed radio galaxies. A few regions of the diffuse emission show a steep spectral index of $\alpha \sim -2$. These regions could trace AGN fossil plasma that has been reaccelerated (or revived) by shocks and turbulence related to the ongoing merger event. A candidate radio halo is located near the peak of the X-ray emission, labeled CH. The complexity of the various radio structures in the vicinity prevents us from measuring its properties.

A.10. PSZ2 G123.66+67.25, Abell 1622

The *Chandra* X-ray image shows that the cluster consists of two subclusters (see Fig. A.10). The main subcluster has a large X-ray extent (∼1 Mpc) and low surface brightness. A smaller, more concentrated subcluster is located to its south. Given the overall roundish morphology of both components, the cluster is likely in a pre-merging state. A additional small substructure is seen to the SW of the southern subcluster. PSZ2 G123.66+67.25 has a temperature of 4.76 ± 0.87 keV and is classified as a non-cool core by Morandi et al. (2015).

No megaparsec-scale diffuse emission is detected in this z = 0.2838 cluster. A bright tailed radio galaxy (A) is found in the northern part of the main subcluster, with the tail bending eastward about 200 kpc north of its optical counterpart. A patch of radio plasma (B) with an LLS of 250 kpc is found to the south of the northern subcluster. A compact radio source is located just north of this diffuse source, but there is no clear connection

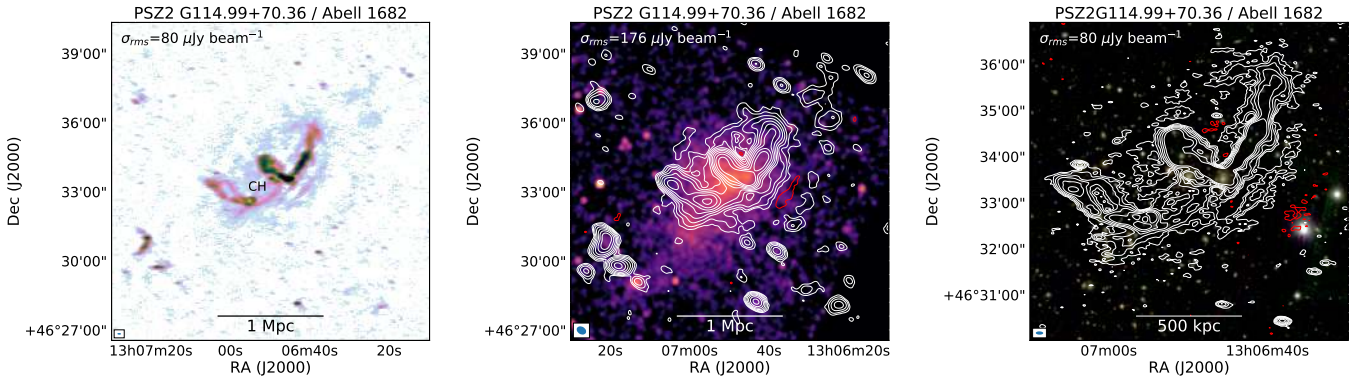

Fig. A.9. PSZ2 G114.99+70.36, Abell 1682. *Left*: robust −0.5 radio image. *Middle*: *Chandra* X-ray image with 10″ tapered radio contours. *Right*: optical image with robust −0.5 image radio contours. For more details, see the caption of Fig. 5.

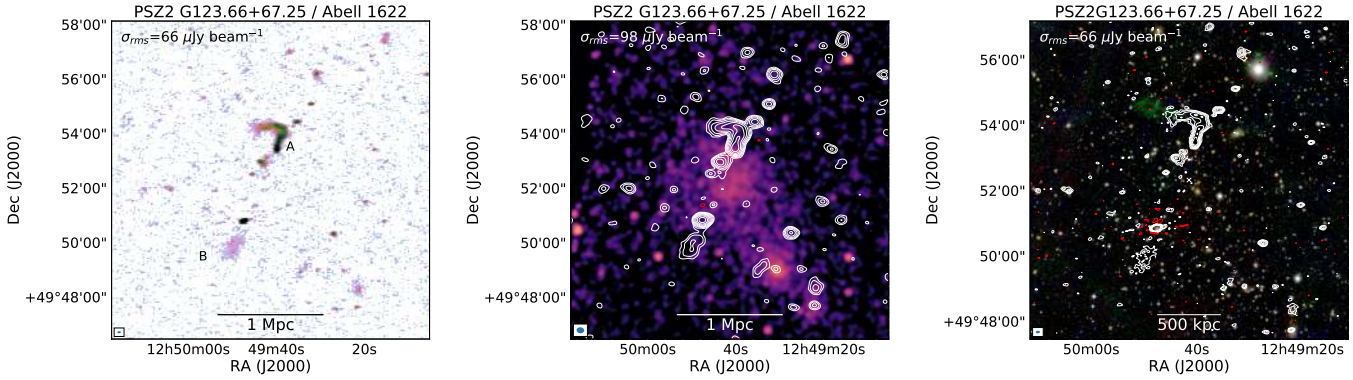

Fig. A.10. PSZ2 G123.66+67.25, Abell 1622. *Left*: robust −0.5 radio image. *Middle*: *Chandra* X-ray image with 10″ tapered radio contours. *Right*: optical image with robust −0.5 image radio contours. For more details, see the caption of Fig. 5.

visible in our high-resolution images. We speculate that this diffuse source is AGN fossil plasma that originated from the compact radio source.

A.11. PSZ2 G136.92+59.46, Abell 1436

The LOFAR image displays compact radio emission associated with the BCG. The *XMM-Newton* image reveals an elongated low-surface-brightness cluster (see Fig. A.11). Optical Pan-STARRS images show the BCG to have a double nucleus. Additional radio emission is detected south of the BCG. Given that this emission connects to the BCG, it likely originated from the BCG. No diffuse radio emission is detected in this cluster.

A.12. PSZ2 G143.26+65.24, Abell 1430

The LOFAR images reveal the presence of diffuse emission in this cluster, which is located at $z = 0.3634$ (see Fig. A.12). The LOFAR observations are discussed in more detail in Hoeft et al. (2020), so we only give a brief overview of the main findings. The diffuse emission extends over a region of about 5′ by 2.5′, with the emission being elongated in the E-W direction. The angular extent corresponds to a physical size of 1.5 Mpc by 0.8 Mpc. Our LOFAR image also reveals two tailed radio galaxies, labeled A and B (Fig. A.12). An optical image displays two subclusters. The western subcluster corresponds to the main structure seen in the *Chandra* X-ray image, while the eastern cluster is much fainter in the *Chandra* image. The radio emission spans the full region between the main western subcluster and the smaller eastern subcluster. Given the clear correspondence between the radio and X-ray emission of the western subcluster and the large extent of the diffuse emission, we classify the western part of the diffuse radio emission as a giant radio halo. We measure $S_{144} = 29.8 \pm 6.6$ mJy for the radio halo from our fitting. We note that this value might be affected by the diffuse emission around the eastern subcluster since it partly overlaps with the radio halo from the western subcluster. The nature of the diffuse emission around the eastern subcluster is not fully clear, but it could be a radio bridge (for a discussion on this, see Hoeft et al. 2020). The disturbed character of the cluster, both in optical and X-ray images, indicates that the cluster is undergoing a merger event, consistent with the presence of a giant radio halo. A possible source of seed electrons for the radio halo could be the tail of source A since it blends into the halo emission.

A.13. PSZ2 G144.33+62.85, Abell 1387

No diffuse radio emission is detected in this cluster. Two BCGs seem to be present in this cluster based on optical Pan-STARRS images (see Fig. A.13). A distorted tailed radio galaxy is associated with one of the two BCGs.

A.14. PSZ2 G151.62+54.78

No diffuse emission is detected in this cluster (see Fig. A.14). However, the observations for this cluster were affected by bad ionospheric conditions, compromising the image quality.

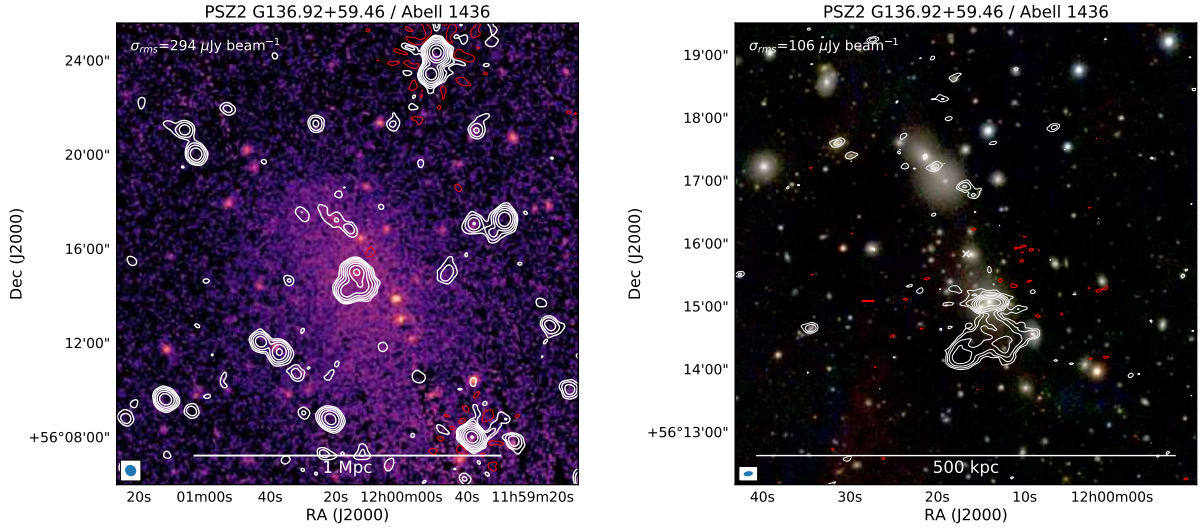

Fig. A.11. PSZ2 G136.92+59.46, Abell 1436. *Left*: *XMM-Newton* X-ray image with 10″ tapered radio contours. *Right*: optical image with robust −0.5 image radio contours. For more details, see the caption of Fig. 5.

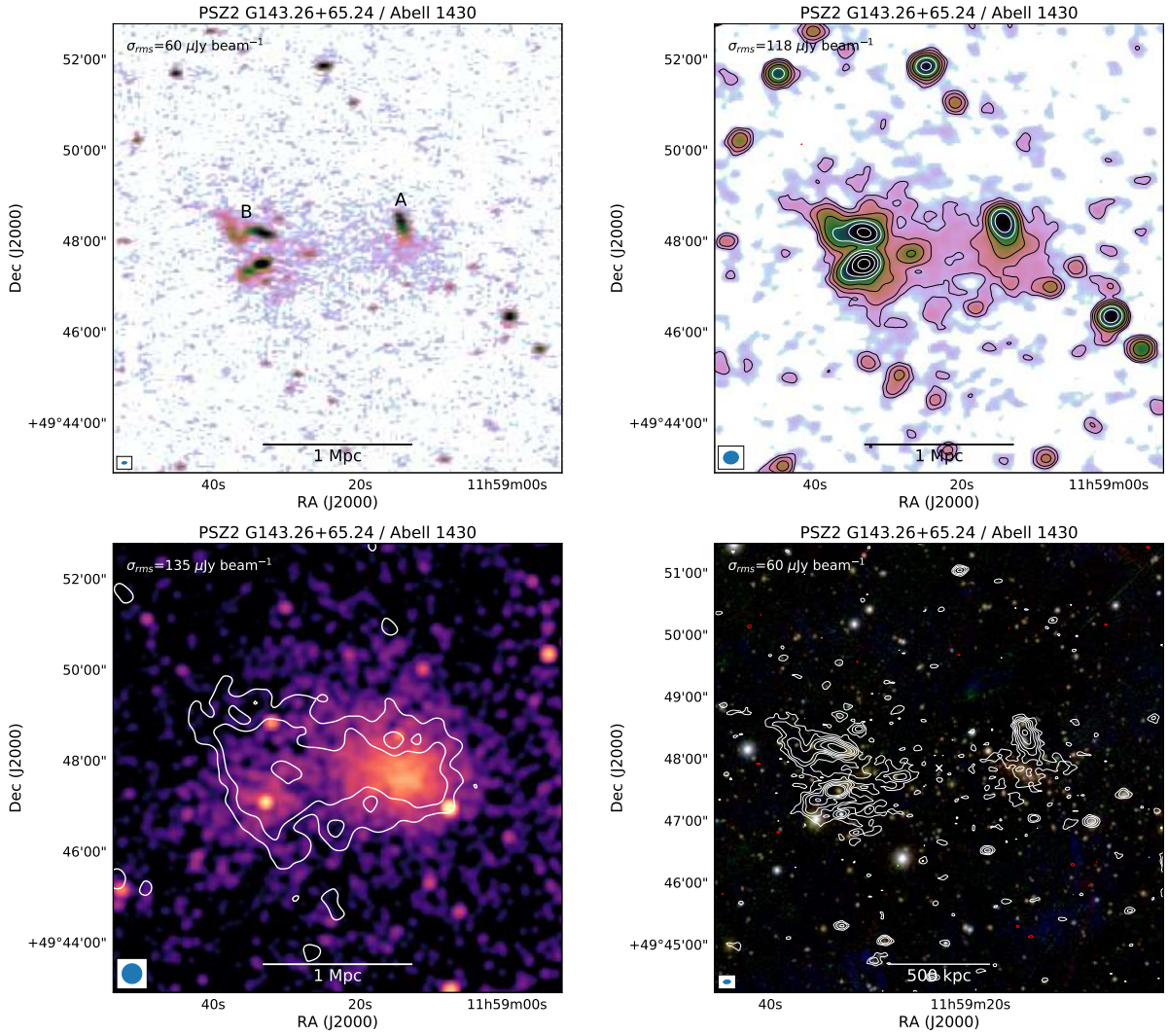

Fig. A.12. PSZ2 G143.26+65.24, Abell 1430. *Top left*: robust −0.5 radio image. *Top right*: 10″ tapered radio image. *Bottom left*: *Chandra* X-ray image with 15″ tapered radio contours (compact sources were subtracted). *Bottom right*: optical image with robust −0.5 image radio contours. For more details, see the caption of Fig. 5.

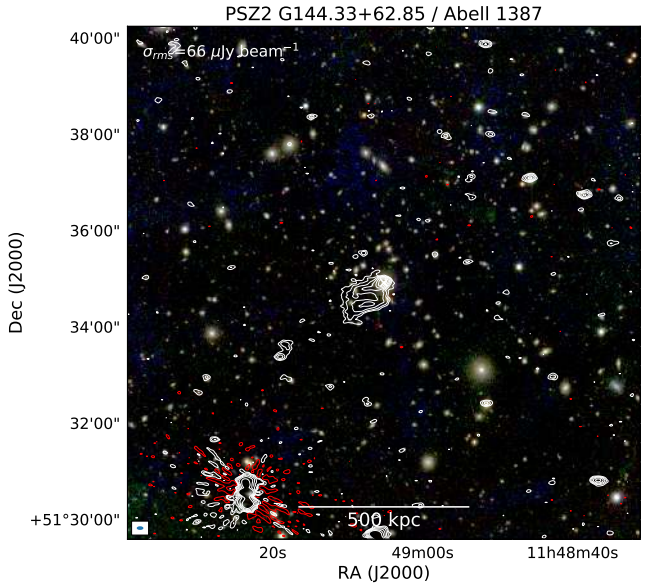

Fig. A.13. PSZ2 G144.33+62.85, Abell 1387. Optical image with robust −0.5 image radio contours. For more details, see the caption of Fig. 5.

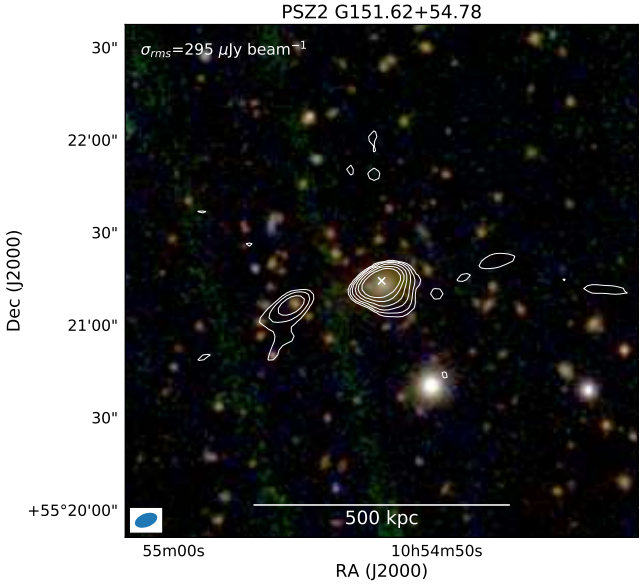

Fig. A.14. PSZ2 G151.62+54.78. Optical image with robust −0.5 image radio contours. For more details, see the caption of Fig. 5.

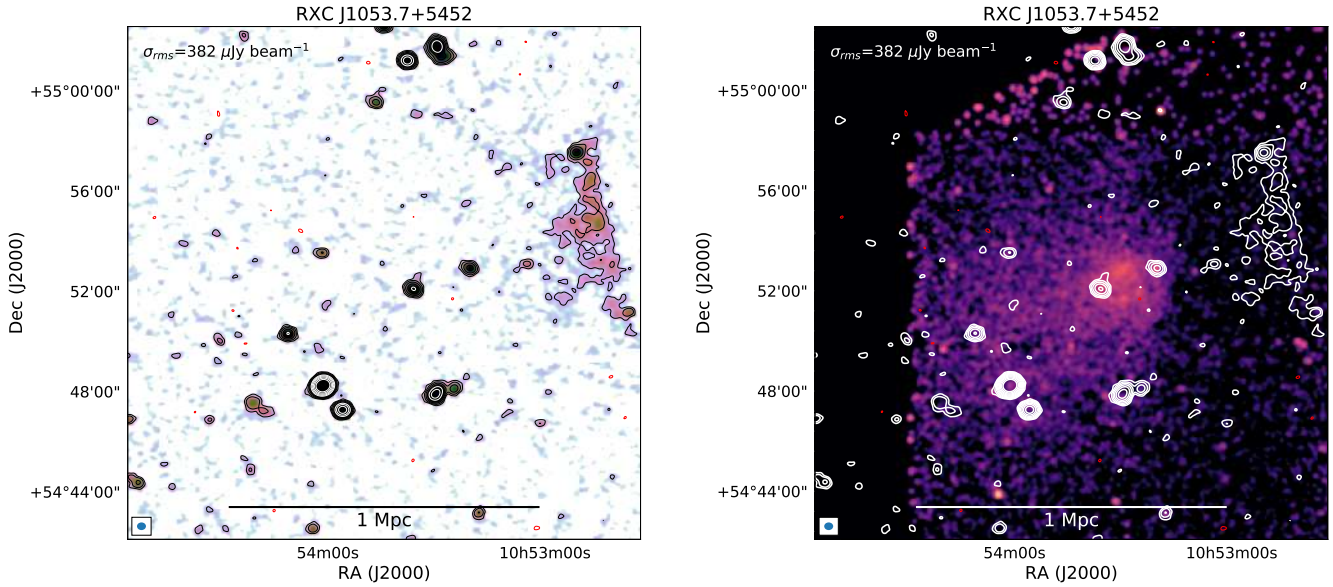

Fig. A.15. RXC J1053.7+5452. *Left*: 10″ tapered radio image. *Right*: *Chandra* X-ray image with 10″ tapered radio contours. For more details, see the caption of Fig. 5.

A.15. RXC J1053.7+5452

Peripheral diffuse radio emission in this cluster was first reported by Rudnick & Lemmerman (2009) and subsequently studied by van Weeren et al. (2011). *Chandra* and Suzaku observations presented by Itahana et al. (2017) show that the cluster is undergoing a merger event. The peripheral radio source is classified as a relic.

The main LOFAR pointing on this source (P164+55) had to be discarded as it was affected by bad ionospheric conditions. Hence the noise levels in our images are higher than for other clusters. Despite the higher noise, the relic is clearly detected in our LOFAR images (Fig. A.15), and the source has a similar appearance as in the Westerbork Synthesis Radio Telescope (WSRT) observations presented in van Weeren et al. (2011). In the LOFAR image, the relic has an LLS of about 0.75 Mpc. A hint of an extension is visible from the northern tip of the relic (near a compact source) toward the west and north. Combining the LOFAR flux density measurement with the one obtained from the WSRT, we obtain $\alpha = -1.17 \pm 0.11$, which is typical for radio relics.

A.16. Abell 1615

This cluster hosts a complex distorted tailed radio galaxy that is related to the BCG. This source has a largest extent of 450 kpc. An optical image with radio contours overlaid is shown in Fig. A.16.

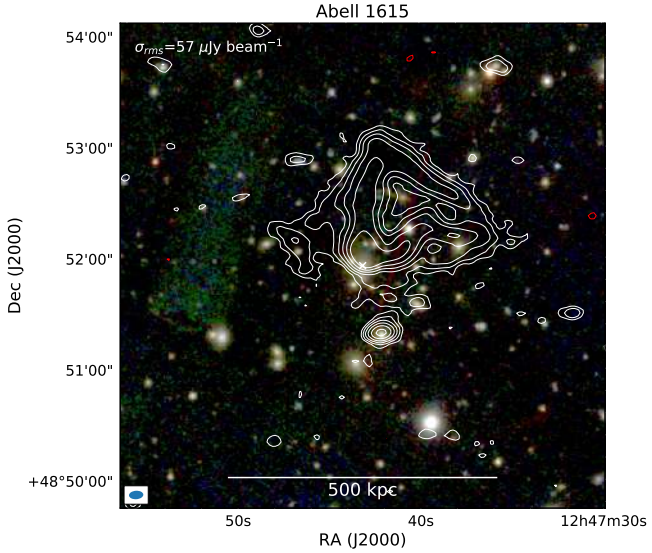

Fig. A.16. Abell 1615. Optical image with robust −0.5 image radio contours. For more details, see the caption of Fig. 5.

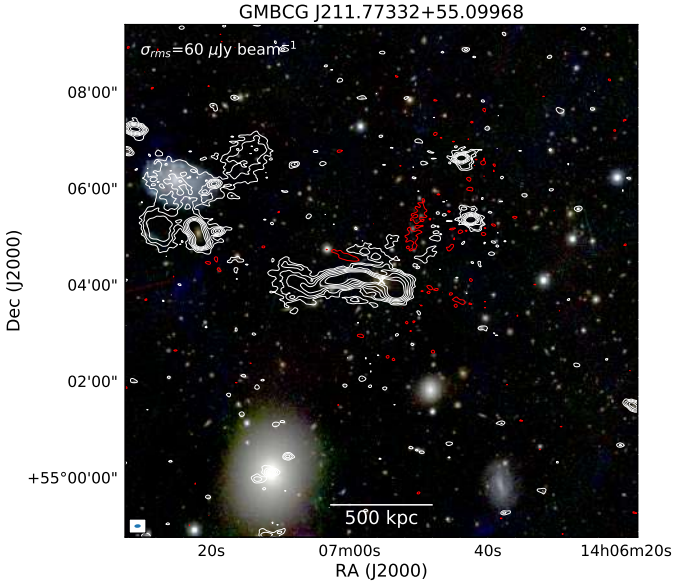

Fig. A.17. GMBCG J211.77332+55.09968. Optical image with robust −0.5 image radio contours. For more details, see the caption of Fig. 5.

A.17. GMBCG J211.77332+55.09968

This cluster hosts a large 600 kpc asymmetric radio galaxy that is associated with the BCG. Extended radio emission is also found NW of the BCG (see Fig. A.17). This emission is composed of three distinct radio sources: a compact double-lobed source, an extended double-lobed source, and a foreground spiral galaxy.

A.18. MaxBCG J173.04772+47.81041

Extended radio emission, likely related to AGN activity from an elliptical galaxy, is detected in the northern part of the cluster. An optical image with radio contours overlaid is shown in Fig. A.18.

A.19. WHL J132615.8+485229

Elongated radio emission that seems to originate from a tailed radio galaxy south of the cluster center is detected (see Fig. A.19). This emission extends all the way to the BCG.

A.20. WHL J134746.8+475214

This cluster hosts complex extended radio emission on scales of 500 kpc, which seems to be related to AGN activity. An optical image with radio contours overlaid is shown in Fig. A.20.

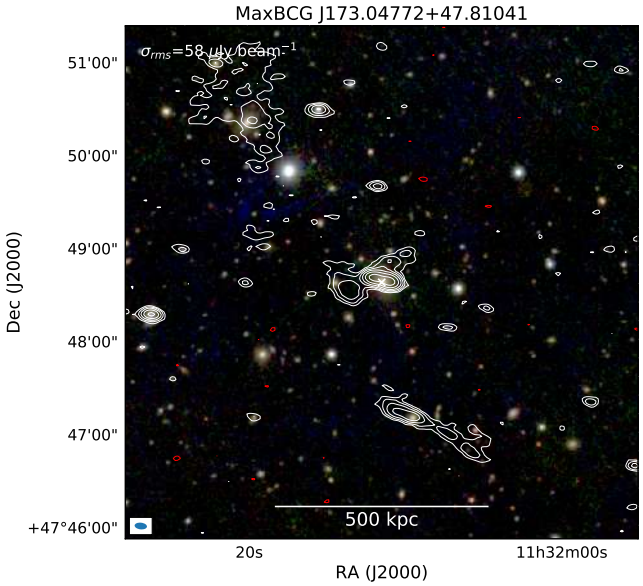

Fig. A.18. MaxBCG J173.04772+47.81041. Optical image with robust −0.5 image radio contours. For more details, see the caption of Fig. 5.

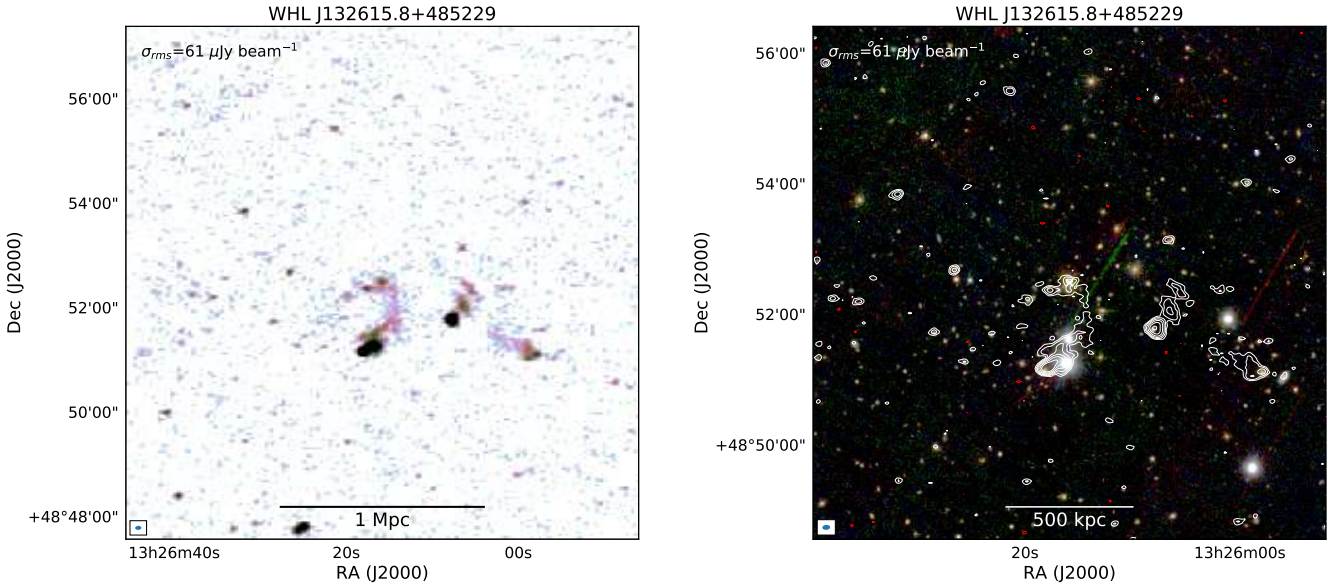

Fig. A.19. WHL J132615.8+485229. *Left*: robust −0.5 image radio image. *Right*: optical image with robust −0.5 image radio contours. For more details, see the caption of Fig. 5.

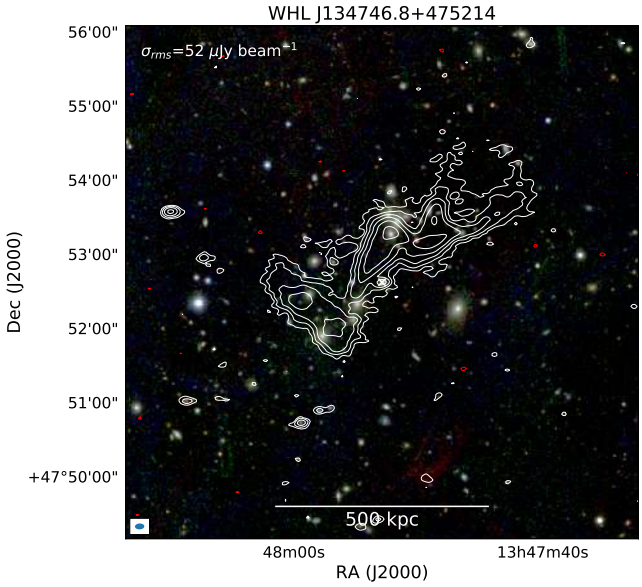

Fig. A.20. WHL J134746.8+475214. Optical image with robust −0.5 image radio contours. For more details, see the caption of Fig. 5.

Appendix B: Radio image properties

In Table B.1 we provide an overview of the image rms noise levels ($\sigma_{\rm rms}$) and the beam sizes.

Table B.1. Radio image properties.

Cluster	rms noise (μJy beam^{-1})	Beam size ($''\times''$, $^\circ$)
PSZ2 G080.16+57.65	134	9.5 × 4.8, 95
PSZ2 G084.10+58.72	78	9.6 × 4.5, 101
PSZ2 G086.93+53.18	113	9.5 × 4.4, 106
PSZ2 G087.39+50.92	123	7.9 × 4.3, 98
PSZ2 G088.98+55.07	90	10.2 × 4.8, 108
PSZ2 G089.52+62.34	68	8.3 × 4.7, 91
PSZ2 G095.22+67.41	66	8.0 × 4.8, 93
PSZ2 G096.14+56.24	168	8.5 × 4.4, 105
PSZ2 G098.44+56.59	78	8.4 × 4.5, 99
PSZ2 G099.86+58.45	66	8.1 × 4.5, 91
PSZ2 G106.61+66.71	52	7.2 × 4.6, 94
PSZ2 G107.10+65.32	138	7.3 × 4.9, 91
PSZ2 G111.75+70.37	68	10.3 × 3.8, 95
PSZ2 G114.31+64.89	85	7.3 × 4.7, 94
PSZ2 G114.99+70.36	80	9.7 × 4.2, 89
PSZ2 G118.34+68.79	70	8.9 × 4.4, 96
PSZ2 G123.66+67.25	66	7.7 × 4.6, 96
PSZ2 G133.60+69.04	64	7.6 × 4.6, 93
PSZ2 G135.17+65.43	78	7.5 × 4.5, 91
PSZ2 G136.92+59.46	106	9.0 × 4.7, 98
PSZ2 G143.26+65.24	60	8.0 × 4.7, 95
PSZ2 G144.33+62.85	66	8.4 × 4.5, 90
PSZ2 G145.65+59.30	70	7.5 × 4.9, 93
PSZ2 G150.56+58.32	87	8.1 × 4.8, 92
PSZ2 G151.62+54.78	295	7.6 × 4.3, 111
PSZ2 G156.26+59.64	89	8.0 × 4.7, 103
RXC J1053.7+5452	245	8.4 × 4.8, 92
Abell 1156	57	8.0 × 4.7, 89
Abell 1314	71	8.8 × 4.9, 89
Abell 1615	57	7.8 × 4.6, 94
MaxBCG J173.04772+47.81041	58	8.0 × 4.3, 84
NSC J143825+463744	102	8.5 × 4.8, 96
GMBCG J211.77332+55.09968	60	7.9 × 4.4, 94
WHL J125836.8+440111	84	8.5 × 5.0, 85
WHL J122418.6+490549	62	7.7 × 4.8, 93
WHL J124143.1+490510	58	7.6 × 4.6, 94
WHL J132226.8+464630	67	8.5 × 4.1, 95
WHL J132615.8+485229	61	7.1 × 4.5, 94
WHL J133936.0+484859	56	7.3 × 4.8, 92
WHL J134746.8+475214	52	7.6 × 4.8, 93